

Combining micro- and macroscopic probes to untangle single-ion and spatial exchange anisotropies in a $S = 1$ quantum antiferromagnet

Jamie Brambleby^{1‡}, Jamie L. Manson^{2,3*}, Paul A. Goddard¹, Matthew B. Stone⁴, Roger D. Johnson^{5,6}, Pascal Manuel⁶, Jacqueline A. Villa², Craig M. Brown³, Helen Lu⁷, Shalinee Chikara⁷, Vivien Zapf⁷, Saul H. Lapidus⁸, Rebecca Scatena⁹, Piero Macchi⁹, Yu-sheng Chen¹⁰, Lai-Chin Wu¹⁰ and John Singleton^{7,8}

¹*Department of Physics, University of Warwick,
Gibbet Hill Road, Coventry CV4 7AL, United Kingdom*

²*Department of Chemistry and Biochemistry, Eastern Washington University, Cheney, WA 99004, U.S.A.*

³*NIST Center for Neutron Research, National Institute of Standards and Technology, Gaithersburg, MD 20899, U.S.A.*

⁴*Quantum Condensed Matter Division, Oak Ridge National Laboratory, Oak Ridge, TN 37831, U.S.A.*

⁵*University of Oxford, Department of Physics, The Clarendon Laboratory,
Parks Road, Oxford, OX1 3PU, United Kingdom*

⁶*ISIS Pulsed Neutron Source, STFC Rutherford Appleton Laboratory,
Didcot, Oxfordshire OX11 0QX, United Kingdom*

⁷*National High Magnetic Field Laboratory, MS-E536,
Los Alamos National Laboratory, Los Alamos, NM 87545, U.S.A.*

⁸*X-ray Sciences Division, Advanced Photon Source,
Argonne National Laboratory, Argonne, IL 60439, U.S.A.*

⁹*Department of Chemistry and Biochemistry, University of Bern, 3012 Bern, Switzerland*

¹⁰*ChemMatCARS, Advanced Photon Source, Argonne National Laboratory, Argonne, IL 60439, U.S.A.*

The magnetic ground state of the quasi-one-dimensional spin-1 antiferromagnetic chain is sensitive to the relative sizes of the single-ion anisotropy (D) and the intrachain (J) and interchain (J') exchange interactions. The ratios D/J and J'/J dictate the material's placement in one or other of three competing phases: a Haldane gapped phase, a quantum paramagnet and an XY-ordered state, with a quantum critical point at their junction. We have identified $[\text{Ni}(\text{HF})_2(\text{pyz})_2]\text{SbF}_6$, where $\text{pyz} = \text{pyrazine}$, as a candidate in which this behavior can be explored in detail. Combining neutron scattering (elastic and inelastic) in applied magnetic fields of up to 10 tesla and magnetization measurements in fields of up to 60 tesla with numerical modeling of experimental observables, we are able to obtain accurate values of all of the parameters of the Hamiltonian [$D = 13.3(1)$ K, $J = 10.4(3)$ K and $J' = 1.4(2)$ K], despite the polycrystalline nature of the sample. Density-functional theory calculations result in similar couplings ($J = 9.2$ K, $J' = 1.8$ K) and predict that the majority of the total spin population of resides on the Ni(II) ion, while the remaining spin density is delocalized over both ligand types. The general procedures outlined in this paper permit phase boundaries and quantum-critical points to be explored in anisotropic systems for which single crystals are as yet unavailable.

I. INTRODUCTION

The possibility of arranging interacting magnetic moments in chains or planes has excited theorists and experimentalists alike for many years. The pioneering work by Kosterlitz and Thouless on XY-like spins in two dimensions^{1,2}, and by Haldane on integer-spin chains^{3,4} has had far-reaching implications, culminating in the award of the 2016 Nobel Prize in Physics⁵. More recently, interest in predicting and controlling the magnetic ground state of $S = 1$ quantum magnets has been fueled by the realization of a myriad of magnetic phases in a series of metal-organic coordination compounds. This includes the observation of field-induced Bose-Einstein condensation in $\text{NiCl}_2\text{-4SC}(\text{NH}_2)_2$ [6–8], as well as the development of a Haldane phase in both $[\text{Ni}(\text{C}_2\text{H}_8\text{N}_2)_2\text{NO}_2]\text{ClO}_4$ [9] and $[\text{Ni}(\text{HF}_2)(3\text{-Clpy})_4]\text{BF}_4$ ($\text{Clpy} = \text{C}_5\text{H}_4\text{NCl} = \text{chloropyridine}$) [10–12]. Ground-state diversity is attributable to the interplay between the single-ion anisotropy (D) and Heisenberg spin-exchange interactions (J) in these materials, which are both determined (in part) by the lattice geometry¹². The flexibility offered by the crystal

structures of quasi-one dimensional coordination polymers renders them ideal systems to advance our understanding of the quantum-critical phenomena associated with $S = 1$ systems.

The magnetic ground state of a quasi-one-dimensional (Q1D) $S = 1$ antiferromagnet (AFM) is particularly sensitive to both the precise nature of D and its strength compared to that of the intrachain Heisenberg spin-exchange interaction¹⁰. The magnetic properties in a magnetic field ($B \approx \mu_0 H$) are summarized by the Hamiltonian

$$\mathcal{H} = \sum_{\langle i,j \rangle} J \mathbf{S}_i \cdot \mathbf{S}_j + \sum_{\langle i,j' \rangle} J' \mathbf{S}_i \cdot \mathbf{S}_{j'} + \sum_i [D(S_i^z)^2 + g\mu_B \mathbf{S}_i \cdot \mathbf{B}], \quad (1)$$

where \mathbf{S} is the spin of each ion (i), $\langle i,j \rangle$ denotes a sum over nearest neighbors, J' is the strength of the interchain interaction, a primed index in the summation describes the interaction with a nearest neighbor in an adjacent chain and g is the isotropic g -factor.

Unlike classical systems, ideal $S = 1$ chains ($J' = 0$) are vulnerable to strong quantum fluctuations¹¹, which can have a profound influence on the magnetic ground state and act to suppress long-range order. Quantum Monte-Carlo (QMC) simulations predict that for easy-plane anisotropy a Haldane ground state gives way to quantum paramagnetism (QP) as the D/J ratio increases, while the effects of J' are to alleviate the quantum disorder and induce an XY -AFM (or Néel if $D = 0$) ordered phase¹⁰. The three magnetic phases are expected to converge at a quantum critical point (QCP) [13], located at $D/J = 0.97$ for purely 1D chains¹². Therefore, the ability to measure J , J' and D precisely, in addition to obtaining an unambiguous experimental determination of the magnetic ground state in real systems, is a crucial step towards testing the theoretical predictions of quantum phenomena in Q1D $S = 1$ chains. However, as we now describe, this has proved challenging in the case of polycrystalline samples, particularly for those systems in which the exchange and anisotropy energies are similar in magnitude. It can often take time to hone synthetic methods sufficiently to obtain single crystals large enough for many measurement techniques. Therefore it is frequently the newest, most exciting families of materials that are most difficult to characterize.

In the absence of a magnetic field and strong spin-exchange interactions, systems described by Eqn. 1 are dominated by single-ion anisotropy. This energy term acts to remove the spin-microstate degeneracy of paramagnetic Ni(II) ions ($m_s = 0, \pm 1$) and is dependent upon both the metal-ligand electronic structure and the spin-density distribution. For hexa-coordinated Ni(II) coordination complexes, this zero-field splitting (ZFS) of energy levels can result in a singlet ($D > 0$) or doublet ground state with D -values that have been found to span the range $-32 \leq D \leq 20$ K [14 and 15]. So long as the Ni \cdots Ni spin-exchange interactions are weak, the D -value in complexes of this type may be characterized by magnetic susceptibility, magnetization, and heat capacity measurements. However, a reliable estimation of both the size *and* sign of D in polycrystalline samples is only possible via these techniques if one can apply magnetic fields of a sufficient strength to significantly align the spins¹⁶. Electron-spin resonance (ESR) is also frequently used to determine the anisotropy and can work well for powdered samples, but only provided the frequency-field combination that matches the ZFS can be achieved.

For exchange-coupled systems, the sensitivity of bulk thermodynamic probes to the spin correlations further complicates the extraction of a unique value for the single-ion anisotropy. A resolution to this problem is offered by a microscopic probe, such as inelastic neutron scattering (INS), which is well suited to differentiating the effects of spin-exchange interactions from those of single-ion anisotropy. The origin of spin excitations (spin-wave or crystal-field levels) may be discriminated by their wave-vector (\mathbf{Q}) and energy-transfer (E) dependence¹⁷. In the past, successful treatment of INS data

has relied on instances of D -only models (ignoring J), as found in high-nuclearity Mn(III) complexes^{18,19}, J -only models (ignoring D) in some Co(II) complexes²⁰⁻²² or $J > D$ as determined in Q1D $\text{MnCl}_2(\text{urea})_2$ [23]. To the best of our knowledge, analysis of powder INS spectra has not been successfully tested in multi-parameter systems where $D \approx J$ until now. Without INS data, density-functional theory (DFT) is often implemented to validate thermodynamic parameters according to a prescribed Hamiltonian (such as Eqn. 1). The results, however, are sensitive to the basis set employed and require experimental support if one is to have confidence in the outcome²⁴⁻²⁶.

Here we describe a complete experimental procedure to determine the H, T phase diagram and all of the parameters of the spin Hamiltonian of $[\text{Ni}(\text{HF}_2)(\text{pyz})_2]\text{SbF}_6$, despite the lack of suitable single crystals. This material is composed of linear HF_2^- pillars that mediate an intrachain Ni—Ni exchange coupling (J), while bridging pyrazine ligands provide four equivalent interactions (J') to neighboring chains²⁷. The material enters an AFM ordered phase below 12.2 K and exhibits $D/J \approx 1$ along with a strong spatial exchange anisotropy (predicted from DFT to be $J'/J \approx 0.1$) [27]. It therefore provides a rare opportunity to study the magnetic properties of a system close to the three competing Q1D ground states.

Below the ordering temperature, elastic neutron scattering of $[\text{Ni}(\text{HF}_2)(\text{pyz})_2]\text{SbF}_6$ reveals that the zero-field magnetic structure is that of a 3D XY -AFM ground state. Based on this result, the anisotropic critical field observed in powder magnetization measurements can then be interpreted within an easy-plane, mean-field picture to initially estimate values of $D = 13.1(3)$ K and $n\langle J \rangle = 22.1(2)$ K (n = number of magnetic nearest neighbors and $\langle J \rangle$ = average spin-exchange interaction strength). Applying Eqn. 1 in SPINW²⁸, we model powder INS spin-wave spectra to deconvolute the two distinct AFM contributions to $n\langle J \rangle$ to yield $J = 10.4(3)$ K and $J' = 1.4(2)$ K that we assign to Ni—FHF—Ni and Ni—pyz—Ni interactions, respectively. Given these parameters, we find good agreement with the predictions of QMC calculations for the low-temperature phase and this result is used to explain the form of the field-temperature phase diagram revealed by heat capacity and magnetization measurements. We compare these parameters to those obtained from low-field magnetic susceptibility measurements and demonstrate the shortcomings in modeling these data in the absence of other information. Lastly, we provide a detailed analysis of the spin-density distribution and exchange-coupling constants as predicted by periodic DFT calculations.

II. EXPERIMENTAL METHODS

A. Design strategy

The tunability offered by metal-organic systems renders them ideal testbeds for which to investigate numerous quantum theories relevant to reduced-dimensionality physics. Our current endeavors are focused on $M(\text{II})$ -based [$M = \text{Co}$ ($S = \frac{3}{2}$), Ni ($S = 1$), Cu ($S = \frac{1}{2}$)] coordination polymers, self-assembled from strong charge-assisted H-bonds (*e.g.*, $\text{F}\cdots\text{H}\cdots\text{F}$) [10, 11, 27, 29–37]. Weaker O-H \cdots F types have also been examined^{38–44}. The use of crystal engineering to manage such interactions is a promising path forward in the experimental search for exotic phases of quantum matter. Among the various Ni(II) systems reported thus far, $[\text{Ni}(\text{HF}_2)(\text{pyz})_2]\text{SbF}_6$ ($\text{pyz} = \text{pyrazine}$)²⁷, α - and β -polymorphs of $[\text{Ni}(\text{HF}_2)(\text{pyz})_2]\text{PF}_6$ and $[\text{Ni}(\text{HF}_2)(3\text{-Clpy})_4]\text{BF}_4$ have been synthesized and characterized^{10,11,27,29}. The latter compound forms isolated Q1D Ni—FHF—Ni chains with bent and asymmetric HF_2^- bridges^{10,11}. Moreover, the suppressed long-range magnetic order (LRO) and $D/J \approx 1$ are unique to this material, as it is the only Ni(II)-chain proximate to the $D/J = 0.97$ QCP, which separates Haldane, XY-AFM, and QP phases¹².

In $[\text{Ni}(\text{HF}_2)(\text{pyz})_2]X$, the presence of additional, albeit weak, interchain Ni—pyz—Ni exchange pathways promote LRO^{27,29} below temperatures ≈ 6 K ($X = \alpha\text{-PF}_6$), 7 K ($X = \beta\text{-PF}_6$), and 12.2 K ($X = \text{SbF}_6$). For each compound, a substantial zero-field splitting (ZFS) is also anticipated due to the existing NiN_4F_2 core; *e.g.*, an easy-plane $D = 20$ K has been determined for Q1D $\text{Ni}(\text{SiF}_6)(\text{vinim})_4$ ($\text{vinim} = 1\text{-vinylimidazole}$)¹⁵.

B. Synthesis

All reagents were obtained from commercial suppliers and used as received. Plasticware was used throughout the entire synthetic process⁴⁵. In a typical synthesis, NiF_2 (1.775 mmol, 302.0 mg) was dissolved separately in 3 mL of aqueous-HF (48–51 % by weight) while NH_4HF_2 (1.775 mmol, 106.5 mg), LiSbF_6 (1.775 mmol, 431.8 mg), and pyrazine (3.550 mmol, 283.7 mg) were dissolved together in a separate beaker containing 2 mL of aqueous HF and 1 mL H_2O . The NiF_2 solution was slowly mixed with the ligands to give a green solution that was covered with a perforated wax film to allow slow evaporation of the solvent. On standing at room temperature for 3 weeks, a blue powder formed on the bottom and walls of the beaker. The solid was collected by vacuum filtration, washed with 2 mL of H_2O , 2 mL of ethanol, and 2 mL of diethyl ether to assist drying. A pale blue powder, consisting of microcrystalline plates ($10 \times 10 \times 2 \mu\text{m}^3$ in average size), was obtained in high yield (> 80 %) based on Ni(II) content). Further details are available in the Supplementary Information⁴⁶. While these microcrys-

tals were suitable for the synchrotron X-ray structural study they were much too small for single-crystal thermodynamic and neutron-scattering measurements.

For the neutron-scattering experiments, synthesis of a partially deuterated phase of $[\text{Ni}(\text{HF}_2)(\text{pyz-d}_4)_2]\text{SbF}_6$, was necessary to reduce the large incoherent scattering cross-section due to protons (*i.e.* the ^1H nuclei). The synthesis was carried out as described above, except pyz was replaced by pyz-d₄. To produce a 1.8 g sample, suitable amounts of HF(aq) and other reagents were used accordingly. X-ray powder diffraction patterns and magnetic susceptibility data were found to be very similar for the hydrogenated and deuterated phases.

C. Microcrystal X-ray diffraction

Experiments were conducted on the ChemMatCARS 15-ID-B beamline of the Advanced Photon Source (APS) at Argonne National Laboratory (ANL). A microcrystal of $[\text{Ni}(\text{HF}_2)(\text{pyz})_2]\text{SbF}_6$ measuring $10 \times 10 \times 2 \mu\text{m}^3$ was selected from a bulk sample using a cryo-loop and mounted on a Bruker D8 fixed-chi X-ray diffractometer equipped with an APEX II CCD area detector. The sample was cooled to 15(2) K using a He-cryojet. Synchrotron radiation with a beam energy of 32.2 keV ($\lambda = 0.38745 \text{ \AA}$) was used, and the beam size at the sample was $0.1 \times 0.1 \text{ mm}^2$. The distance between sample and detector was set at 60 mm. A total of 720 frames were collected at $\theta = -5^\circ, 140^\circ$ and 180° with the ϕ -angle scanned over 180° at intervals of 0.5° . Data collection and integration were performed using the APEX II software suite. Data reduction employed SAINT⁴⁷. Resulting intensities were corrected for absorption by Gaussian integration (SADABS)⁴⁸. The structural solution (XT) [49] and refinement (XL) [50] were carried out with SHELX software using the XPREP utility for the space-group determination. Considering systematic absences, the crystal structure was solved in the tetragonal space group $P4/nmm$ (#129, origin choice 2) [51]. Pyrazine H-atoms were placed in idealized positions and allowed to ride on the carbon atom to which they are attached. All non-hydrogen atoms were refined with anisotropic thermal displacement parameters.

D. Elastic neutron scattering

Magnetic diffraction patterns were recorded on the WISH diffractometer (ISIS, Rutherford Appleton Laboratory, UK)⁵². As mentioned above, a partially deuterated sample, $[\text{Ni}(\text{HF}_2)(\text{pyz-d}_4)_2]\text{SbF}_6$, of mass 1.8 g was loaded into a cylindrical vanadium can and placed in an Oxford Instruments cryostat with a base temperature of 1.5 K. Diffraction data were collected over the temperature interval 1.5 – 20 K, with long counting times (8 hrs) at 1.5 K and 20 K. Intermediate temperature points were measured with an exposure time of 2 hrs. Rietveld refine-

ments were performed using FULLPROF⁵³. All atoms were refined using isotropic thermal displacement parameters.

E. Heat capacity

Heat capacity (C_p) measurements were carried out using a 9 T Quantum Design PPMS, with a 1.91(5) mg powder sample of $[\text{Ni}(\text{HF}_2)(\text{pyz})_2]\text{SbF}_6$ that was pressed into a pellet, secured to a sapphire stage with Apiezon-N grease and held in contact with a large thermal bath. Measurements of C_p were performed using the traditional relaxation method⁵⁴. For this technique, a heat pulse ($\approx 1\%$ of the thermal bath temperature) was applied to the stage and C_p evaluated by measuring the time constant of the thermal decay curve. The heat capacities of the Apiezon-N grease and sample platform were measured separately and subtracted from the total to obtain the heat capacity of the sample.

F. Temperature-dependent linear susceptibility

Linear susceptibility ($M/\mu_0 H$, where M is the magnetization) measurements were made for temperatures in the range $1.9 \leq T \leq 50$ K and fields $\mu_0 H \leq 13$ T using a Quantum Design Physical Property Measurement System (PPMS) equipped with a vibrating sample magnetometer (VSM). A 2 mg powder sample was loaded into a brass holder, and mounted in the VSM transport. The sample was initially cooled in zero applied field to $T = 1.9$ K. Data were collected upon warming and corrected for diamagnetic contributions from the sample and background.

G. Pulsed-field magnetization

Measurements of the powder magnetization of $[\text{Ni}(\text{HF}_2)(\text{pyz})_2]\text{SbF}_6$ up to 60 T made use of a 1.5 mm bore, 1.5 mm long, 1500-turn compensated-coil susceptometer, constructed from a 50 gauge high-purity copper wire³³. When the sample is within the coil, the signal voltage V is proportional to dM/dt , where t is time. Numerical integration of V is used to evaluate M . The sample is mounted within a 1.3 mm diameter ampoule that can be moved in and out of the coil. Accurate values of M are obtained by subtracting empty-coil data from that measured under identical conditions with the sample present. The susceptometer was placed inside a ³He cryostat providing a base temperature of 0.5 K. The magnetic field was measured by integrating the voltage induced in a 10-turn coil calibrated by observing the de Haas-van Alphen oscillations of the belly orbits of the copper contained in the susceptometer coil³³.

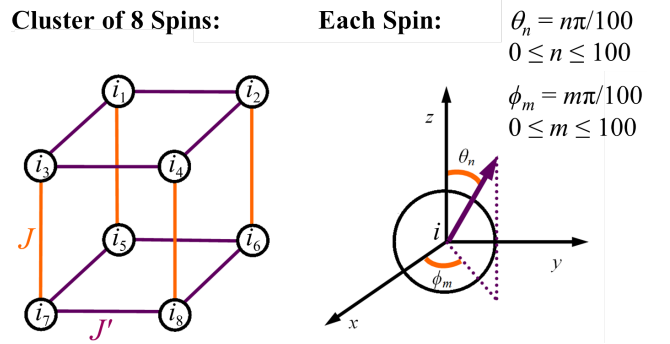


FIG. 1. The 2×2 planar arrangement of Ni(II) ions used in the simulation of the magnetization. Each ion (i) is represented by a vector where the two degrees of freedom are the polar angles θ_n and ϕ_m , each limited to 100 evenly spaced values. J and J' correspond to Ni—FHF—Ni and Ni—pyz—Ni exchange interactions, respectively.

H. Inelastic neutron scattering

Two INS measurements were performed using the disk-chopper spectrometer (DCS) located at the NIST Center for Neutron Research (NCNR)⁵⁵. Both measurements used neutrons of wavelength 3.7 Å to scatter from a 1.8 g, partially deuterated powder sample of $[\text{Ni}(\text{HF}_2)(\text{pyz-d}_4)_2]\text{SbF}_6$ loaded in an aluminum sample can sealed under a helium atmosphere. The first measurement was conducted in zero field to probe the temperature-dependence of INS spectra at $T = 1.6$ K, 10 K, and 20 K. The magnetic spin excitations were examined by subtracting the 20 K (*i.e.* above the ordering temperature) data from the 1.6 K measurement.

Thermodynamic parameters were determined by comparing the measured powder spin-wave spectra against a series of spectra simulated using the SPINW analysis package²⁸, assuming the XY magnetic structure determined by elastic neutron scattering. The second measurement surveyed the magnetic-field dependence of spin excitations at $T = 1.6$ K and 20 K in magnetic fields of $\mu_0 H = 0, 3, 6,$ and 10 T. To account for the time-independent background of the measurements, an overall value of 27 counts per hour per detector was subtracted from the data. This value was not subtracted in cases where data are plotted as the difference between two temperatures or two fields.

III. THEORY, CALCULATIONS AND SIMULATIONS

A. Monte-Carlo simulation of high-field magnetization

We compute the powder-average magnetization of $[\text{Ni}(\text{HF}_2)(\text{pyz})_2]\text{SbF}_6$ using a classical Monte-Carlo routine written in MATLAB⁵⁶. A cluster of 8 ions is ar-

ranged in two sets of 2×2 planes (Fig. 1) and the magnetic moment of each ion (i) is represented by a classical vector, constrained by the polar angles θ_i and ϕ_i . The spins are coupled via the Hamiltonian of Eqn. 1, for which periodic boundary conditions are applied. The zero-field spin configuration uses the results of elastic neutron scattering (see below) starting with collinear moments, antiferromagnetically coupled to all neighbors and oriented within the xy -planes. The simulation considered how the lowest-energy configuration of spins changes in a magnetic field. This was repeated for twenty-one evenly spaced angles (α) between the magnetic field and the hard-axis (z) and for values in the range $0 \leq \alpha \leq 180^\circ$.

For a fixed value of α , the magnitude of the field is increased from 0 to 60 T in $\mu_0 \Delta H = 0.3$ T steps. Following the field increment, the energy of the cluster was minimized with respect to the angles (θ_n, ϕ_m) using the Metropolis Monte Carlo algorithm⁵⁷. First, θ for one spin is changed to a new random value and the energy of the new configuration calculated from Eqn. 1. If the energy decreases, the change is accepted. If the energy is raised by an amount ΔE , the change is accepted with a probability $\exp(-\Delta E/k_B T)$, otherwise the move is rejected. Next, the reorientation of the angle ϕ of the spin is considered in the same way as before applying the routine to the remaining seven moments in the cluster. This process is repeated 2000 times for a particular value of magnetic field. Once complete, the magnetization parallel to the applied field, $\mathbf{M}(\alpha, \mathbf{H}) \cdot \frac{\mathbf{H}}{|\mathbf{H}|}$, was extracted and recorded. The powder average magnetization at a particular magnetic field, $M_{\text{avg}}(H)$, is then determined by

$$M_{\text{avg}}(H) = \frac{\sum_{\alpha} \left[\mathbf{M}(\alpha, \mathbf{H}) \cdot \frac{\mathbf{H}}{|\mathbf{H}|} \right] \sin \alpha \Delta \alpha}{\sum_{\alpha} \sin \alpha \Delta \alpha} \quad (2)$$

Owing to the condition which allows the energy to be raised during a field step, the final spin configuration will be within an energy of $k_B T$ from the true ground state. Hence, the parameter T plays the role of temperature. Here, T is chosen to be 0.1 K, so as to find the most probable ground state spin configuration.

B. DFT calculation of spin density

The exchange-coupling constant J can be related to the energy difference between states with different spin multiplicities^{58–61}. For this purpose, accurate unrestricted wave functions for the ferromagnetic (FM) and AFM spin states are required. We have investigated the FM and several combinations of AFM states, imposing a coupling only along Ni—FHF—Ni or the Ni—pyz—Ni directions, or along both, in order to estimate J and J' as well as the total coupling.

The CRYSTAL14 code⁶² was used to perform DFT calculations with periodic boundary conditions on relevant FM and AFM phases of $[\text{Ni}(\text{HF}_2)(\text{pyz})_2]\text{SbF}_6$ using the B3LYP hybrid functional. The basis set was

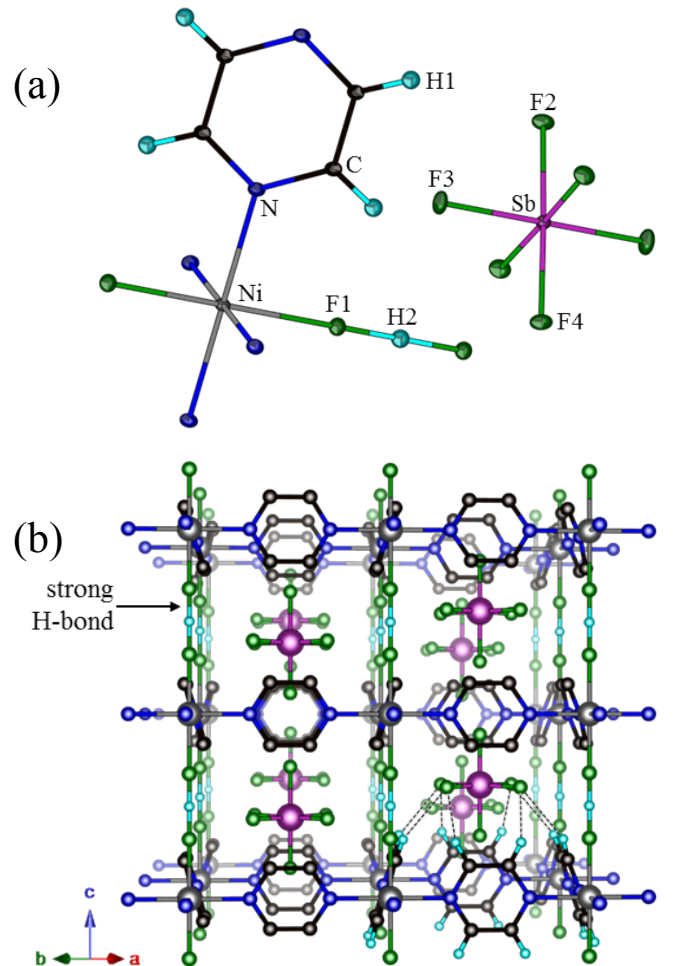


FIG. 2. Structure of $[\text{Ni}(\text{HF}_2)(\text{pyz})_2]\text{SbF}_6$ determined at $T = 15$ K by microcrystal X-ray diffraction. (a) Thermal ellipsoid plot (50 % displacement parameters) showing the basic building blocks and atom-labeling scheme. Ni(II) ions have 4-fold rotational symmetry while the HF_2^- constituent atoms H2 and F1 have respective site symmetries of $4m2$ and $2mm$. (b) Polymeric metal-organic framework including interstitial SbF_6^- ions. Each Sb atom occupies the 4-fold rotation axis that lies parallel to the c -direction but the centroid of the SbF_6^- ion is displaced about 0.6 Å relative to the ideal body-centered position. For clarity, only the lower right quadrant depicts the weak hydrogen bonds that exist between pyz ligands and the SbF_6^- ion ($\text{H1} \cdots \text{F3} = 2.478$ Å; dashed lines).

$6-31G(d,p)$ [63] for all of the atoms except for Sb which utilized $3-21G(d)$ [64]. Electron-spin and charge-density maps were calculated using the routines in CRYSTAL14 and the spin-atomic distribution was determined using Mulliken partitioning⁶⁵.

TABLE I. X-ray crystallographic details and refinement results for $[\text{Ni}(\text{HF}_2)(\text{pyz})_2]\text{SbF}_6$. Here, F = amplitude of structure factor of reflection and σ = standard deviation of F . The R -factors are given by $R = \sum |F_{\text{obs}} - F_{\text{calc}}| / \sum |F_{\text{obs}}|$, $R_{\text{int}} = \sum |F_{\text{obs}}^2 - F_{\text{calc}}^2| / \sum |F_{\text{obs}}^2|$ and $wR = (\sum w |F_{\text{obs}} - F_{\text{calc}}|^2 / \sum |w F_{\text{obs}}|^2)^{1/2}$, where the sums run over all data points and w is a weighting factor. S is the goodness of fit. Errors in parentheses are one standard deviation.

Parameter (units)	
Facility/beamline	Advanced Photon Source/15-ID-B
Chemical formula	$\text{C}_8\text{H}_9\text{N}_4\text{F}_8\text{NiSb}$
Crystal system	Tetragonal
Space group	$P4/nmm$ (#129; origin choice 2)
Temperature (K)	15(2)
Wavelength, λ (Å)	0.38745
a, b, c (Å)	9.8797(2), 9.8797(2), 6.4292(1)
Volume (Å ³)	627.54(2)
Formula units per unit cell, Z	2
Absorption coefficient, μ (mm ⁻¹)	1.98
Crystal size (μm^3)	$10 \times 10 \times 2$
Data collection	
No. of measured reflections [$F > 3\sigma(F)$]	74100
No. of independent reflections	2851
No. of observed reflections	2484
R_{int}	0.0780
Spherical-atom refinement	
R [$F > 3\sigma(F)$], R_{all} , wR , S	0.0318, 0.0427, 0.0612, 1.111
No. parameters	36

IV. RESULTS AND DISCUSSION

A. Low-temperature chemical and magnetic structure

Microcrystal X-ray diffraction. The 15 K structure (Fig. 2) of $[\text{Ni}(\text{HF}_2)(\text{pyz})_2]\text{SbF}_6$ was solved in the tetragonal space group $P4/nmm$ based on the single-crystal X-ray diffraction data. Full details of the structural refinement are given in Table I. Selected bond lengths and bond angles can be found in Table II. Each Ni(II) ion is axially-coordinated to two F1 atoms at a distance of 2.076(1) Å [the atom labelling scheme is shown in Fig. 2(a)]. The F1 atoms belong to bridging HF_2^- ligands that form one-dimensional linear Ni—FHF—Ni chains along the c -axis with respective F1 \cdots F1 and Ni \cdots Ni separations of 2.276(1) Å and 6.4292(1) Å. These linkages mediate an intrachain interaction through σ -bond magnetic coupling as established by experiment and DFT (see below). Pyrazine ligands join the Ni(II) ions [Ni—N = 2.098(1) Å] along the [110] and $[\bar{1}\bar{1}0]$ directions to produce two-dimensional (2D) square sheets in the ab -plane [Fig. 2(b)], with equal Ni—Ni separations of 6.9860(2) Å, and provide the interchain interactions. The slight difference in Ni—F1 and Ni—N bond lengths results in a weakly compressed octahedral NiN_4F_2 coordination environment. Trans-coordinated pyz ligands are counter-rotated and tilt away from the NiN_4 plane by 73.04(4)°. The ordering of the pyz ligands in $[\text{Ni}(\text{HF}_2)(\text{pyz})_2]\text{SbF}_6$ contrasts the two-fold positional disorder encountered in the related quasi-two-dimensional (Q2D) layered coordination polymers $\text{NiZ}_2(\text{pyz})_2$ ($Z = \text{Cl, Br, I, NCO}$), which

crystallize in the $I4/mmm$ space group^{66,67}. The structurally related material, $\text{Ni}(\text{NCS})_2(\text{pyz})_2$, has monoclinic symmetry and no apparent pyz disorder⁶⁶.

Interstitial sites within the $[\text{Ni}(\text{HF}_2)(\text{pyz})_2]^+$ framework are occupied by charge-compensating SbF_6^- ions. Significant close contacts of 2.478 Å exist between pyrazine H-atoms and equatorial Fs from the SbF_6^- [Fig. 2(b); dashed lines]. These weak C—H \cdots F hydrogen bonds probably constrain the pyz ligands to a single configuration and are unlikely to contribute to any additional magnetic exchange mechanism.

Elastic neutron scattering. The chemical structure of $[\text{Ni}(\text{HF}_2)(\text{pyz-d}_4)_2]\text{SbF}_6$ was refined at 1.5 and 20 K using Rietveld analysis as implemented in FULLPROF (Fig. S1) [53]. Structural parameters derived from the microcrystal X-ray study of the hydrogenated phase were used as initial input. As anticipated, the deuterated material was found to be isostructural to the hydrogenated phase and the magnetic properties of the two compounds were found to be very similar based on magnetic susceptibility measurements. Unit-cell parameters derived from neutron scattering can be found in Table III, whereas Table II compares bond lengths and bond angles provided by the X-ray and neutron experiments.

Examining the difference in scattered neutron intensity obtained at 1.5 and 20 K [Fig. 3(a)] reveals three distinct Bragg peaks at approximately 3.94 Å, 4.19 Å, and 7.85 Å that do not overlap any nuclear peaks. These are attributed to long-range antiferromagnetic order of Ni(II) moments in the material. Indexing of the superlattice peak at 7.85 Å requires doubling of the chemical unit cell along the c -axis. This indicates that the intrachain

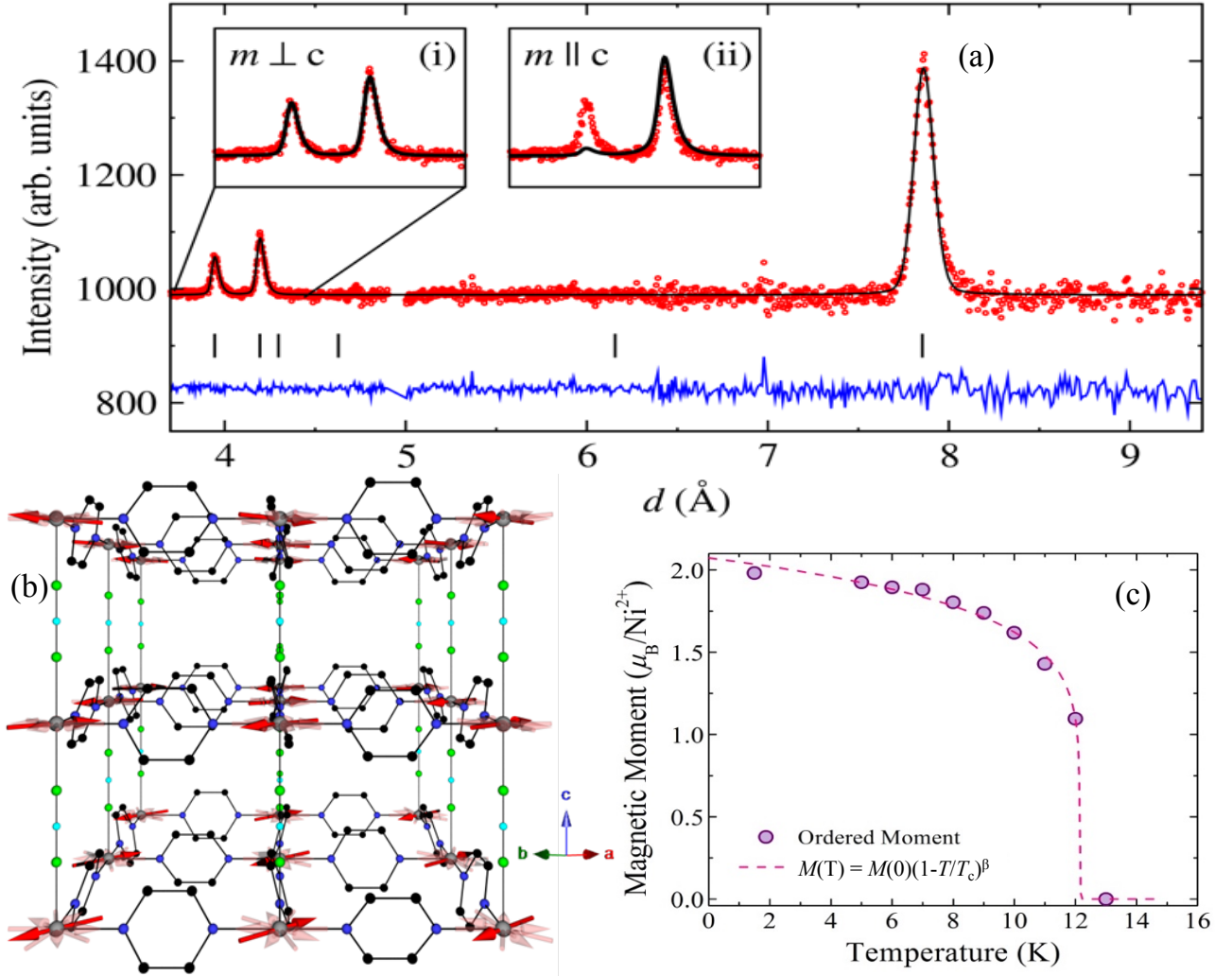


FIG. 3. Elastic neutron scattering data. (a) Magnetic diffraction pattern (red points) for $[\text{Ni}(\text{HF}_2)(\text{pyz-d}_4)_2]\text{SbF}_6$ obtained by subtracting data collected at 20 K from that collected at 1.5 K (see Supplementary Information (SI)⁴⁶). The fitted spectrum (black line) has the Ni(II) moment lying in the ab -plane. Bragg peaks are indicated by ticks and the blue line is the difference between the data and the fit. The insets show a comparison of the model calculated with the moments perpendicular (i) or parallel (ii) to the c -axis. (b) Zero-field magnetic structure (omitting pyz Hs and SbF_6^-). Collinear XY -ordered Ni(II) magnetic moment vectors are indicated by red arrows. (c) T -dependence of the ordered Ni(II) magnetic moment. The power law fit yields⁷⁰ $T_c = 12.13(7)$ K and $\beta = 0.141(1)$.

interaction along the HF_2^- bridge is AFM in nature, as was also found to be the case in the isostructural Cu(II) and Co(II) congeners²⁷. Thus, the magnetic unit cell corresponds to a propagation vector $\mathbf{k} = (0, 0, \frac{1}{2})$ referenced to reciprocal lattice vectors based on the chemical unit cell.

Symmetry analysis and structure-factor calculations (see Fig. S1) demonstrated that the d -spacing positions of the magnetic-diffraction intensities were only consistent with a magnetic structure comprised of collinear spins anti-parallel to their nearest-neighbors (G-type). Two spin directions are then unique by symmetry: (i) spins orthogonal to the crystallographic c -axis; or (ii) spins parallel to the c -axis.

These two scenarios were tested through refinement of

the respective magnetic structure models against the diffraction data. It was found that only scenario (i) quantitatively predicts the relative intensities of all of the measured magnetic Bragg peaks, as is clearly shown in Fig. 3(a), and corroborated by the respective agreement factors (R_{mag}) of 5.89 % and 18.6 %. General comparison between calculated (F_c^2) and observed (F_o^2) structure factors for preferred configuration (i) show very good correlation (Table IV). We therefore conclude that $[\text{Ni}(\text{HF}_2)(\text{pyz})_2]\text{SbF}_6$ exhibits the 3D XY -AFM ground state depicted in Fig. 3(b).

At $T = 1.5$ K, the experimentally determined Ni(II) magnetic moment has a magnitude of $2.03(7)\mu_B$, which is very close to the full moment expected for an $S = 1$ ion, $gS\mu_B = 2.08\mu_B$, given the published²⁷ powder-average g -

TABLE II. Comparison of selected bond lengths (\AA) and bond angles (degrees) for $[\text{Ni}(\text{HF}_2)(\text{pyz})_2]\text{SbF}_6$ as determined by the microcrystal X-ray and neutron powder diffraction studies. (*Compared to Σ_{vdw} of 2.94 \AA for a pair of fluorine atoms.)

	X-rays ($T = 15$ K)	Neutrons ($T = 20$ K)	Neutrons ($T = 1.5$ K)
Ni-N	2.098(1)	2.095(2)	2.096(2)
Ni-F1	2.076(1)	2.067(6)	2.070(6)
H2...F1	1.138(1)	1.149(6)	1.146(6)
F1...F1*	2.276(1)	2.297(9)	2.292(9)
C-N	1.338(1)	1.338(3)	1.338(3)
C-C	1.391(2)	1.403(3)	1.402(3)
C-H1/D1	0.95	1.071(4)	1.071(4)
Sb-F2	1.869(2)	1.889(4)	1.890(4)
Sb-F3	1.886(1)	1.892(11)	1.893(11)
Sb-F4	1.863(2)	1.771(12)	1.770(13)
Ni...Ni (<i>c</i> -axis)	6.4292(1)	6.4319(2)	6.4318(2)
Ni...Ni [1 1 0; 1 $\bar{1}$ 0]	6.9860(2)	6.9958(1)	6.9956(1)
F1-Ni-F1	180	180	180
N-Ni-N	90, 180	90, 180	90, 180
F1-Ni-N	90	90	90
Ni-F1...H2	180	180	180
Ni-N...N	180	180	180
C-N-C	116.97(9)	116.8(3)	116.8(3)
N-C-H1/D1	119.2	119.1(4)	119.0(4)
F2-Sb-F3	89.27(3)	89.8(4)	89.8(5)
F2-Sb-F4	180	180	180
F1-Ni-N-C	73.04(4)	73.7(1)	73.7(1)

factor. This observed full moment precludes strong quantum fluctuations in the ground state which were prominent in the Q2D Heisenberg $S = \frac{1}{2}$ Cu(II) congener, for which a reduced ordered moment of 0.6(1) μ_B was found³⁰. The differing results can be attributed to the smaller spin-quantum number and strong quantum fluctuations, significantly larger spatial exchange anisotropy, and the lack of single-ion anisotropy in the copper material.

Data plotted in Fig. 3(c) were obtained by fitting the ordered moment to each measured diffraction pattern. The resulting fit of these data to a power law of the form⁷⁰, $M(T) = M(0)[1 - T/T_c]^\beta$, yielded $T_c = 12.13(7)$ K and $\beta = 0.141(1)$. For most systems the critical region in which power-law behavior applies is restricted to $1 - T/T_c < 10^{-2}$ [68]. Sparse data in the vicinity of T_c suggests caution in assigning β to a particular model.

Field-dependent heat capacity and susceptibility. The zero-field heat capacity plotted as C_p/T versus T [Fig. 4(a)] shows a sharp maximum at 12.2(1) K, indicating a transition to long-range order in addition to a sloping background resulting from the phonon contribution. The data for $T \geq 32$ K have been modeled³⁴ with one Debye and two Einstein phonon modes and the resulting fit parameters are tabulated in Table V.

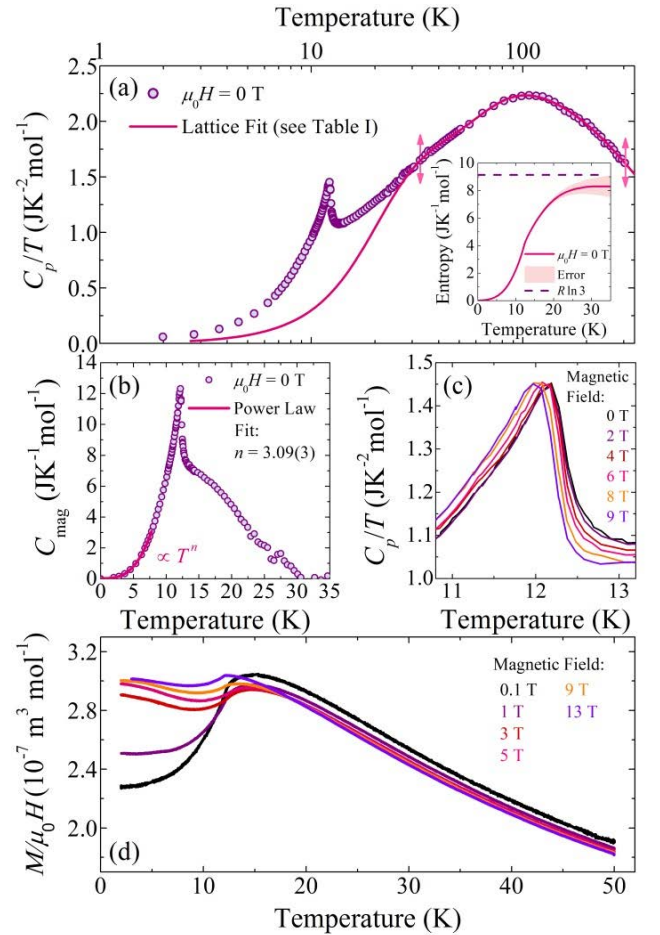


FIG. 4. (a) Ratio of heat capacity to temperature T for $[\text{Ni}(\text{HF}_2)(\text{pyz})_2]\text{SbF}_6$ (points). Data for $T > 32$ K have been fitted (arrows) to a model of one Debye mode and two Einstein modes (line). The inset shows the magnetic entropy up to 35 K where it can be seen to approach the expected value of $R \ln 3$ for $S = 1$ ions. (b) Magnetic heat capacity (C_{mag}) exhibits a broad maximum preceding a sharp transition at 12.2(1) K, indicating the onset of long-range order. Data below 8 K were fitted to a power law, T^n , yielding $n = 3.09(3)$. (c) Field dependence of T_c for magnetic fields $0 \leq \mu_0 H \leq 9$ T. (d) Field-dependent linear susceptibility ($M/\mu_0 H$) versus T for $[\text{Ni}(\text{HF}_2)(\text{pyz})_2]\text{SbF}_6$, showing a broad maximum, the temperature of which is suppressed by increasing field.

The three lattice modes show similar energy scales to those deduced from analogous analysis of the copper³⁴ and cobalt³⁰ isomorphs, which results from the shared structure of this family of compounds. Subtracting the phonon heat capacity from the total measured heat capacity of $[\text{Ni}(\text{HF}_2)(\text{pyz})_2]\text{SbF}_6$, the magnetic heat capacity shows a broad hump that develops on cooling and precedes a transition to long-range order (Fig. 4). This broad feature corresponds to a significant reduction in the spin entropy for $T > T_c$ (inset) and is likely to result from the combination of two mechanisms that restrict the magnetic degrees of freedom of the system: (i) devel-

TABLE III. Refinement details from neutron powder-diffraction data for $[\text{Ni}(\text{HF}_2)(\text{pyz-d}_4)_2]\text{SbF}_6$ at 1.5 K and 20 K. The magnetic propagation vector in reciprocal lattice units (r.l.u.) is k and μ is the refined Ni(II) magnetic moment. The goodness-of-fit parameters $R_F = \sum |I_{\text{obs}}^{\frac{1}{2}} - I_{\text{calc}}^{\frac{1}{2}}| / \sum I_{\text{obs}}^{\frac{1}{2}}$, $R_{\text{Bragg}} = \sum |I_{\text{obs}} - I_{\text{calc}}| / \sum |I_{\text{obs}}|$, where I_{obs} is the observed intensity, I_{calc} is the calculated intensity and the sum runs over all data points. R_{mag} is the equivalent R factor to R_{Bragg} applied to the fit of the magnetic scattering only.

Parameter (units)		
Formula	$\text{C}_8\text{HD}_8\text{N}_4\text{F}_8\text{NiSb}$	$\text{C}_8\text{HD}_8\text{N}_4\text{F}_8\text{NiSb}$
Temperature (K)	20	1.5
Space group	$P4/nmm$	$P4/nmm$
a, b, c (\AA)	9.8936(1), 9.8936(1), 6.4319(2)	9.8933(1), 9.8933(1), 6.4318(2)
Volume (\AA^3)	629.57(2)	629.53(2)
Z	2	2
k (r.l.u.)	–	(0, 0, 1/2)
Order type	–	G-type
μ (μ_B)	–	2.03(7)
WISH detector banks	Bank 2 + Bank 9	Bank 2 + Bank 9
R_F (%)	5.42	5.46
R_{Bragg} (%)	3.64	3.62
R_{mag} (%)	–	5.89 ($m \perp c$), 18.6 ($m \parallel c$)

TABLE IV. Observed and calculated nuclear and magnetic structure factors for $[\text{Ni}(\text{HF}_2)(\text{pyz})_2]\text{SbF}_6$ as determined by the 1.5 K neutron-diffraction study. F_o and F_c correspond to observed and calculated structure values, respectively, for a given d -spacing.

h	k	l	F_o^2	F_c^2 ($\perp c$)	F_c^2 ($\parallel c$)	d -spacing (\AA)
1	0	$\frac{3}{2}$	2.999	2.927	0.431	3.9358
1	2	$\frac{1}{2}$	3.539	3.662	5.079	4.1856
1	0	$\frac{1}{2}$	2.631	2.854	2.241	7.8454

TABLE V. Fitted parameters for the phonon heat capacity of $[M(\text{HF}_2)(\text{pyz})_2]\text{SbF}_6$, where $M = \text{Ni(II)}$, Cu(II) [34] and Co(II) [30]. The simplest lattice model³⁴ required to fit the data included one Debye (D) and two Einstein (E) modes that are each determined by an amplitude (A_i) and characteristic temperature (θ_i) ($i = \text{D, E}$).

	Ni(II)	Cu(II)	Co(II)
A_D ($\text{JK}^{-1}\text{mol}^{-1}$)	123(3)	76(1)	82(1)
θ_D (K)	148(3)	94(8)	80(1)
A_{E1} ($\text{JK}^{-1}\text{mol}^{-1}$)	271(6)	134(4)	174(3)
θ_{E1} (K)	345(7)	208(4)	177(2)
A_{E2} ($\text{JK}^{-1}\text{mol}^{-1}$)	240(6)	191(4)	287(3)
θ_{E2} (K)	860(30)	500(3)	448(6)

opment of XY -anisotropy of the individual Ni(II) moments, as well as (ii) the build-up of AFM spin correlations among neighboring Ni(II) ions dispersed along the Ni—FHF—Ni chains.

For $T \ll T_c$, spin-wave excitations are the dominant contribution to the magnetic heat capacity. The data below 8 K have been represented with a power law T^n , where n has a fitted value of $n = 3.09(3)$. This expo-

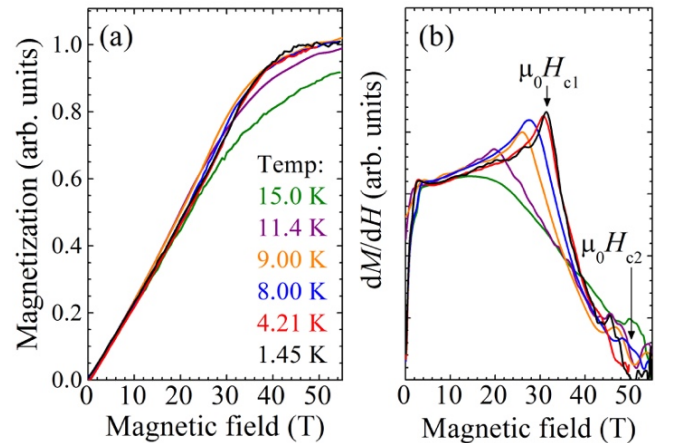


FIG. 5. (a) Magnetization M versus applied magnetic field $\mu_0 H$ for $[\text{Ni}(\text{HF}_2)(\text{pyz})_2]\text{SbF}_6$ measured in pulsed fields for selected $T \leq 15$ K. (b) Differential susceptibility dM/dH versus $\mu_0 H$; such data were used to determine the T dependence of the critical field H_{c1} . The values of H_{c1} and H_{c2} at 1.45 K are shown by arrows.

nent was previously reported for the total sample heat capacity²⁷, but the new results specifically exclude contributions to the measurement from the Debye mode. A T^3 dependence of the heat capacity is expected for an AFM ordered system within which the magnetic excitations (magnons) propagate in three dimensions⁶⁹, which highlights the need to include the effects of J and J' in the analysis of the spin-wave excitation spectra measured from inelastic neutron data (see below).

The field dependence of the heat capacity [$\mu_0 H \leq 9$ T; Fig. 4(c)] and the linear susceptibility [$M/\mu_0 H$; $\mu_0 H \leq 13$ T; Fig. 4(d)] implies that the transition temperature is suppressed in applied magnetic field, as required for an AFM ground state. The overall field dependence is weak

for fields of up to 13 T, owing to the large critical fields in this system, and the high-field portion of the phase diagram was explored using pulsed-field magnetization measurements (see below).

B. Experimental determination of D , J and J'

High-field magnetization. The pulsed-field magnetization of $[\text{Ni}(\text{HF}_2)(\text{pyz})_2]\text{SbF}_6$ at low temperatures shows a slightly concave rise with increasing field and a broadened approach to saturation [Fig. 5(a)]. Two critical fields are identified at 1.45 K, which correspond to an initial increase and subsequent decrease in dM/dH close to 30 T and the point where $dM/dH \rightarrow 0$ near 50 T [Fig. 5(b), arrows]. To interpret the primary features, we adopt a mean-field model for AFM-coupled easy-plane $S = 1$ ions which may be justified based on the ground state determined from elastic neutron scattering (see above). Within this model the saturation field should be anisotropic with an easy plane and a hard axis such that two saturation fields could be observed in the powder data. For fields perpendicular and parallel to the magnetic hard axis, each of these saturation fields (H_{c1} and H_{c2} , respectively) can be calculated by

$$\mu_0 H_{c1} = \frac{2n\langle J \rangle}{g\mu_B} \quad (3)$$

and

$$\mu_0 H_{c2} = \frac{2n\langle J \rangle + D}{g\mu_B} \quad (4)$$

where n is the number of nearest neighbors for each magnetic ion and $\langle J \rangle$ is an average spin-exchange interaction. In a powder measurement of the differential susceptibility, a decrease in dM/dH occurs at H_{c1} once a portion of the sample is saturated. Then, dM/dH continues to decrease to H_{c2} , where no further increase in the magnetization can occur as all Ni(II) moments are aligned with the magnetic field.

The first critical field, H_{c1} for $[\text{Ni}(\text{HF}_2)(\text{pyz})_2]\text{SbF}_6$ is easily identified at all $T < 15$ K (Fig. 5). Combining these critical fields with the heat-capacity results (above), the field-temperature phase diagram can be derived (Fig. 6). The phase boundary for fields applied perpendicular to the magnetic hard-axis (solid lines) is fitted to the expression

$$T_c(H) = T_c(0) \left[1 - \left(\frac{H}{H_{c1}} \right)^{\alpha_1} \right]^{\beta_1}. \quad (5)$$

Fixing $T_c(0) = 12.2$ K, the resultant fitted parameters are $\mu_0 H_{c1} = 31.5(2)$ T, $\alpha_1 = 4.6(4)$, $\beta_1 = 0.56(4)$.

The temperature evolution of the saturation field for fields parallel to the magnetic hard axis ($\mu_0 H_{c2}$) is harder to follow; the dM/dH signal is lowest in this field region and arises from a diminishing proportion of the

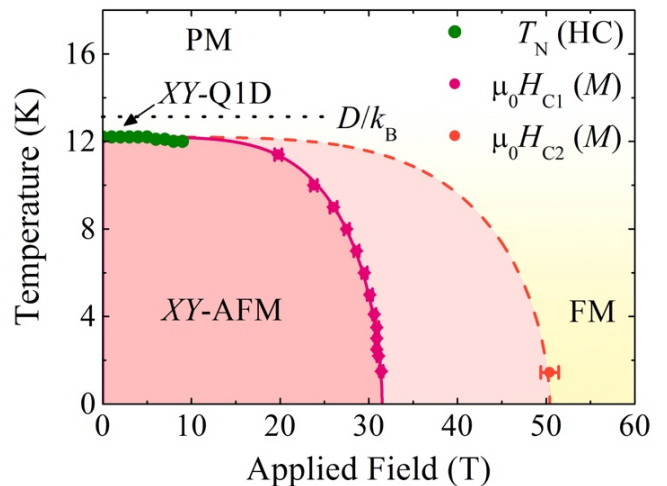


FIG. 6. Field-temperature (H, T) phase diagram for $[\text{Ni}(\text{HF}_2)(\text{pyz})_2]\text{SbF}_6$, mapped out using data from heat capacity (HC) and pulsed-field magnetization (M) measurements. Here, XY-AFM = long-range XY-antiferromagnetic order, FM = fully polarized phase; and XY-Q1D is a region where the moments are antiferromagnetically correlated along the chains, with the Ni(II) moments oriented perpendicular to those chains; H_{c1} (H_{c2}) is the field at which the magnetization saturates when the magnetic field is applied perpendicular (parallel) to the hard axis. The $\mu_0 H_{c1}$ phase boundary (solid line) is modeled using Eqn 5, whilst the $\mu_0 H_{c2}$ boundary (dashed line) is a guide to the eye. The energy scale of the single-ion anisotropy (D) is indicated by a dotted line for reference.

sample as this field is approached. In addition, as the temperature increases, the transition to saturation is broadened further. At the lowest temperatures, however, the saturation field can be identified and is found to be $\mu_0 H_{c2} = 50.4(2)$ T at 1.45 K.

Using these critical fields in conjunction with Eqns. 3 and 4 and the powder average g -value²⁷ of 2.08, we determine $D = 13.2(5)$ K and $n\langle J \rangle \equiv 2J + 4J' = 22.0(2)$ K. To decompose $n\langle J \rangle$ into individual J and J' contributions, we appeal first to a catalog of related coordination polymers that also contain square $[\text{Ni}(\text{pyz})_2]^{2+}$ motifs^{66,71}. From Table VI, we glean an average $J' = 0.9(2)$ K. Applying this to $[\text{Ni}(\text{HF}_2)(\text{pyz})_2]\text{SbF}_6$ leads to $J = 9.2(5)$ K. Therefore, the resultant D/J and J'/J ratios are more than and less than one, respectively, which is consistent with a preliminary DFT study²⁷ used to calculate J' . These parameters are in good agreement with the results of the INS measurements and the Monte-Carlo simulations detailed below.

Using these results, the form of the phase diagram can be interpreted. On cooling the sample from room temperature in zero-field, the sample moves from a paramagnetic (PM) phase to a region within which the Ni(II) moments develop XY-anisotropy (XY-Q1D) and their directions are antiferromagnetically correlated for neighboring ions along the Ni—FHF—Ni chains, with the moments arranged perpendicular to these chains. On

TABLE VI. Review of the exchange interaction strengths mediated through Ni-pyz-Ni linkages (J') for coordination polymers consisting of approximately square $[\text{Ni}(\text{pyz})_2]^{2+}$ plaquettes similar to those found in $[\text{Ni}(\text{HF}_2)(\text{pyz})_2]\text{SbF}_6$. The values listed were obtained by thermodynamic measurements.

System	J' (K)	T_c (K)	Ref.
$\text{NiCl}_2(\text{pyz})_2$	0.49(1)	< 0.08	66
$\text{NiBr}_2(\text{pyz})_2$	1.00(5)	1.8(1)	66
$\text{NiI}_2(\text{pyz})_2$	< 1.19	2.5(1)	66
$\text{Ni}(\text{NCS})_2(\text{pyz})_2$	0.82(5)	1.8(1)	66
$[\text{Ni}(\text{H}_2\text{O})_2(\text{pyz})_2](\text{BF}_4)_2$	1.05(5)	3.0(1)	71

cooling further, there is a magnetic phase transition to an ordered state. We assign this to long-range order with XY moments antiferromagnetically and collinearly aligned to their nearest neighbors. Starting from this ordered phase and applying a magnetic field, the system is driven through a field-induced phase transition to a FM-like phase. This occurs for fields bounded by the range $H_{c1} \leq H \leq H_{c2}$, depending on whether the field is applied perpendicular (H_{c1}) or parallel (H_{c2}) to the z -direction. For powder measurements of the magnetization this anisotropy leads to the slow and broad approach toward saturation.

Inelastic neutron scattering. Figure 7(a-c) shows the measured powder INS energy-momentum transfer spectrum of $[\text{Ni}(\text{HF}_2)(\text{pyz-d}_4)_2]\text{SbF}_6$ in zero-field for $T = 1.6, 10$ and 20 K. As the temperature decreases an upper bound of the spectrum appears at a neutron energy transfer ≈ 3.4 meV. Given that the feature becomes more pronounced on cooling, this T -dependence suggests that it is likely associated with spin-wave formation due to long-range magnetic order. The difference between the $T = 1.6$ K and $T = 20$ K spectra [Fig. 7(d)] reveals the magnetic spectrum more clearly, showing a band of excitations that exists below 3.3 meV. Below 1 meV, the high temperature background is large, leading to an over-subtraction of the data. The energy scale, wave-vector and temperature dependence of the scattering below 1 meV indicate that the large background may be attributed to acoustic phonons that contribute to the scattering intensity at these energies. Furthermore, a small percentage of hydrogen in the sample due to incomplete deuteration could increase the background due to the large incoherent cross-section of the ^1H isotope. For $T < T_c$, magnetic Bragg peaks along $E = 0$ are evident at $|\mathbf{Q}| \approx 0.8 \text{ \AA}^{-1}$, 1.6 \AA^{-1} and 2.0 \AA^{-1} [white arrows in Fig. 7(d)] which is fully consistent with the elastic neutron diffraction patterns.

Figure 8 shows the magnetic-field dependence of the excitation spectrum. For each data set, a $T = 20$ K background measurement at the same applied magnetic field was made and subtracted from subsequent field-dependent data. We found these 20 K spectra to give

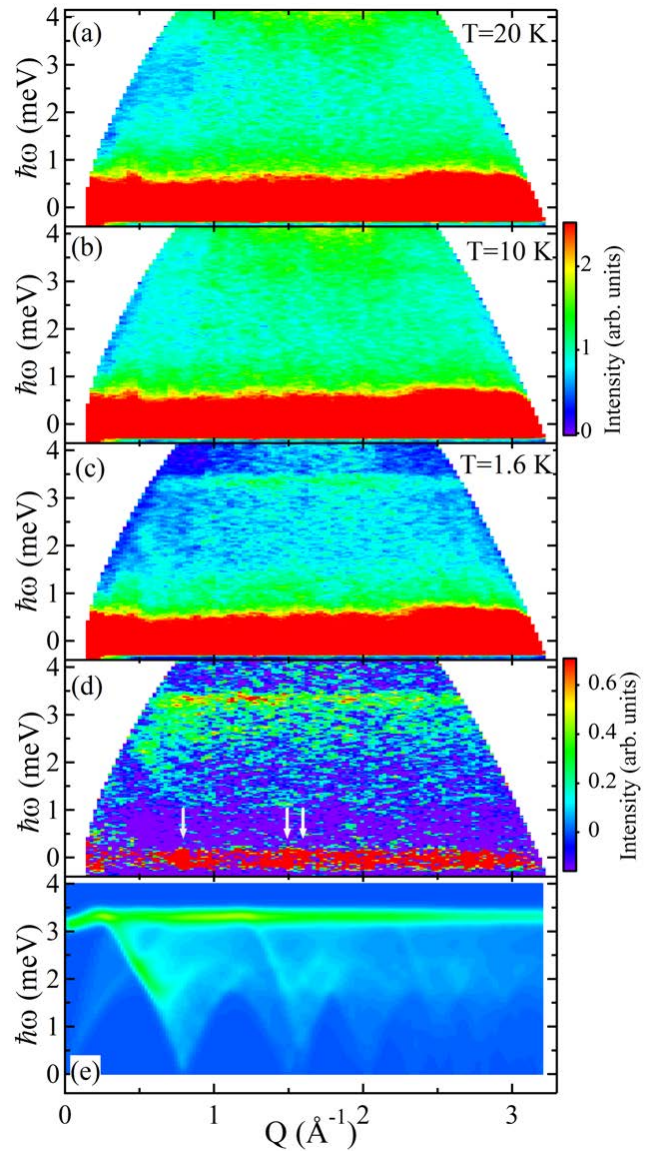


FIG. 7. Intensity contour plots of INS data with no background subtraction for: (a) $T = 20$ K, (b) $T = 10$ K, and (c) $T = 1.6$ K. Panel (d) is the $T = 1.6$ K measurement after subtracting the $T = 20$ K data as a background. The data were binned in units of 0.025 meV and 0.025 \AA^{-1} and then smoothed once with a 3×3 -bin-sized Gaussian kernel. White arrows in panel (d) highlight the locations of prominent magnetic Bragg peaks as validated by the diffraction experiment on WISH [see Fig. 3(a)]. Panel (e) shows the simulated powder INS spectrum for the parameters $D = 13.3(1)$ K, $J = 10.4(3)$ K and $J' = 1.4(2)$ K.

a reasonable representation of the behavior of the paramagnetic phase of our material. The peak in the zero-field spin-wave density-of-states shifts to lower energy transfers as the magnetic field increases. The magnetic Bragg peak at $Q = 0.8 \text{ \AA}^{-1}$ does not shift with increasing magnetic field, indicating that the periodicity of the long-range order does not change with field (see inset of

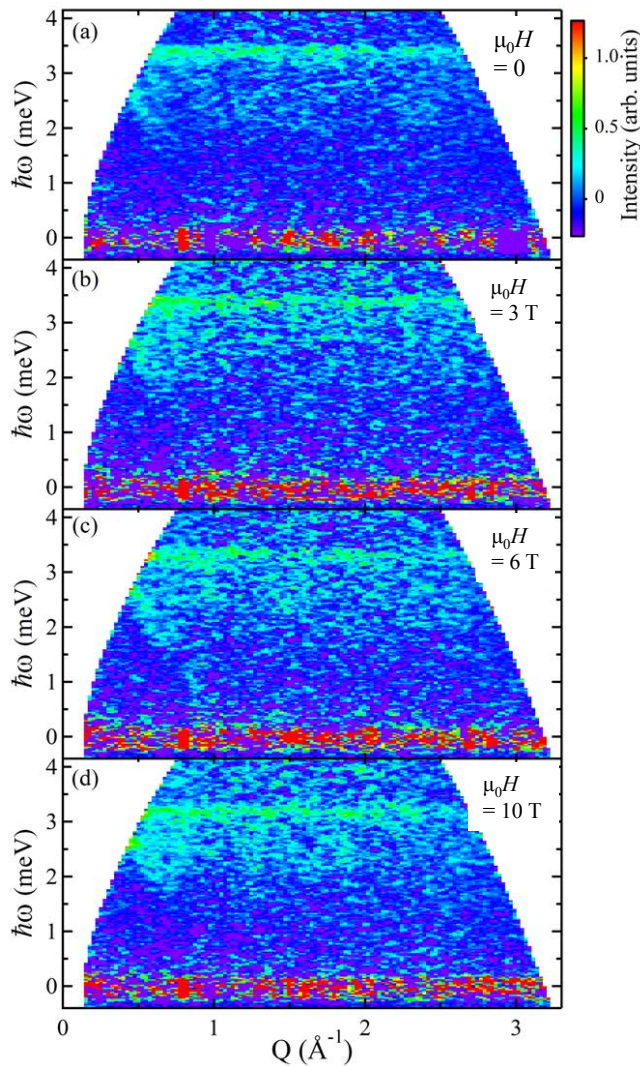


FIG. 8. Background-subtracted magnetic-field dependent INS data obtained at $T = 1.5$ K for (a) $\mu_0 H = 0$, (b) $\mu_0 H = 3$ T, (c) $\mu_0 H = 6$ T, and (d) $\mu_0 H = 10$ T. Data were binned and smoothed in a similar manner to those in Fig. 7. Data measured at $T = 20$ K and at corresponding magnetic fields were used as a paramagnetic backgrounds for each set of data taken at 1.5 K.

Fig. 9). For non-zero magnetic fields, [Fig. 8(b-d)], there is some additional scattering intensity that is present at energies higher than the top of the zero-field spin wave band at 3.4 meV.

Integrating the data from Fig. 8 for momentum transfers in the range $0.8 - 2.5 \text{ \AA}^{-1}$, (Fig. 9) illustrates how the intense portion of the zero-field spin-wave mode at an energy transfer of 3.4 meV softens with the applied magnetic field. There is also an increase in scattering intensity at higher energy transfers with increasing field indicating that the degeneracy of the spin-wave mode is lifted by the field and a portion of the spectrum is moving to larger energy transfers.

With the material well within the ordered magnetic

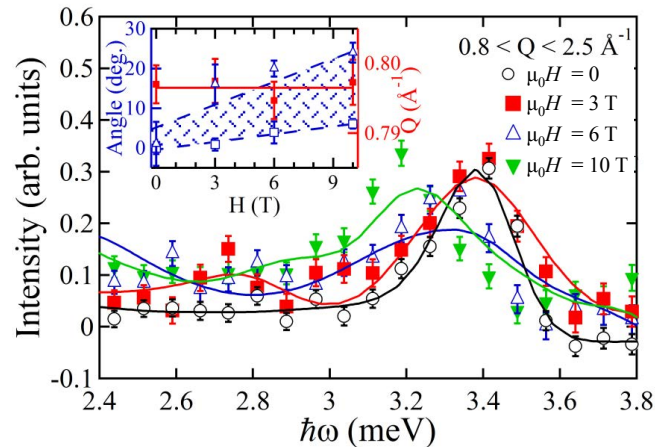


FIG. 9. (Main plot): Background subtracted intensity as a function of energy transfer ($\hbar\omega$) for magnetic fields $\mu_0 H \leq 10$ T. The data correspond to those shown in Fig. 8 integrated between 0.8 and 2.5 \AA^{-1} in wave-vector transfer. The solid lines correspond to the spin-wave calculations discussed in the text; they use a randomly applied magnetic field orientation. (Inset) The open blue triangles correspond to the field-dependent spin reorientations of the Ni(II) moments using the random-field calculation. The open blue squares correspond to the field-dependent spin reorientations of the Ni(II) moments considering only moments applied along the c -axis of the crystal. The shaded area is the range between a linear field-dependent fit to this reorientation angle for each of the models. The solid red squares (right axis) in the inset show the location of the magnetic Bragg peak as a function of H . The solid red line is a fit to a constant value.

phase at $T = 1.6$ K, we modeled the zero-field spectrum shown in Fig. 7(d) using the numerical spin wave calculation package SPINW²⁸. We use the aforementioned zero-field magnetic structure as the basis for all subsequent simulations. The exchange interactions J and J' are included in the model as well as the anisotropy term D as described in Eqn. 1.. A powder-average spin-wave spectrum is calculated for energy transfers between 2 and 4 meV for a large range of values in D , J and J' parameter space. The limited range of energy transfer was used for comparison to avoid the lower energy region due to the acoustic-phonon scattering previously described. Each simulated spin-wave spectrum was directly compared to the measurement and a value of reduced χ^2 was determined for each triplet of energy parameters. Fitting parameters for each simulation included a constant background and an overall multiplicative prefactor to scale the calculated scattering intensity^{72,73}. The best-fit parameters were found from the minimum in reduced χ^2 . Figure 7(e) shows the final simulated spectrum. The resulting terms in the Hamiltonian were determined to be $D = 13.3(1)$ K, $J = 10.4(3)$ K and $J' = 1.4(2)$ K, with D and J falling in the range estimated from thermodynamic measurements. Any potential next-next-nearest neighbor Ni—Ni exchange interaction along the a - and b -axes (*i.e.*, the diagonals of the $[\text{Ni}(\text{pyz})_2]^{2+}$ square plaquettes,

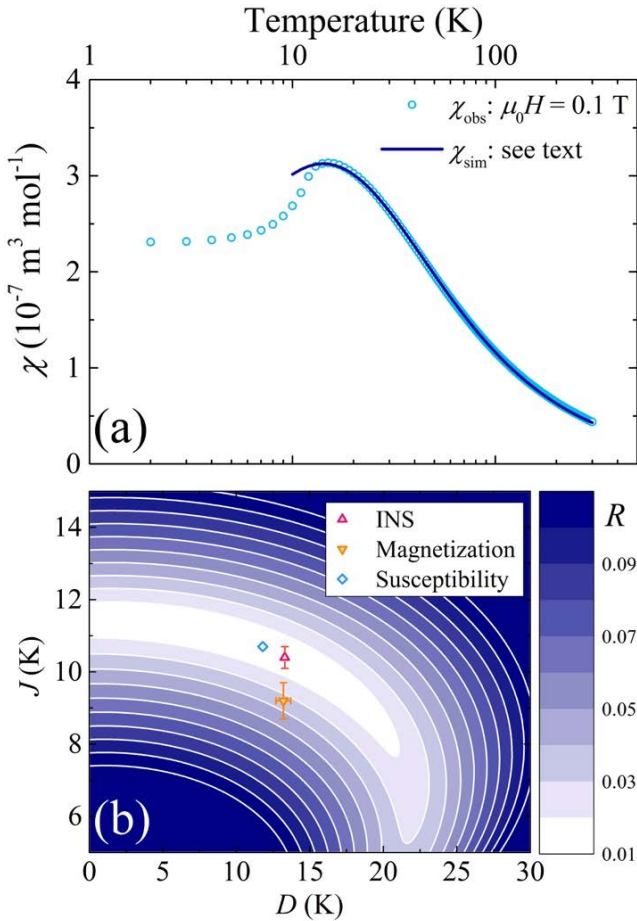


FIG. 10. (a) Magnetic susceptibility χ versus temperature T data for $[\text{Ni}(\text{HF}_2)(\text{pyz})_2]\text{SbF}_6$ ($\mu_0 H = 0.1$ T) interpolated to evenly spaced temperatures in the range $2 \leq T \leq 300$ K, $\Delta T = 1$ K (χ_{obs} , points). (b) Contour plot of the quality factor R in the D, J plane found by comparing the simulated susceptibility (Eqns. 6 and 7) to the measured data using Eqn. 8 (see text for details). The result shows bands of D and J that provide very similar quality fits to the data. The model (χ_{sim}) that yields the minimum value of R (diamond) is displayed as a solid line in panel (a).

see Fig. 2), with a distance of 9.880 \AA , would likely be much smaller than J' and require measurements on single crystals with improved energy resolution to determine accurately.

In addition, we calculated the magnetic-field dependence of the excitation spectrum. For this case, we perform the powder average using a random field direction with the moments tilted by a fixed angle from their zero-field orientation toward the applied magnetic field. We then average this calculated spectrum over 128 random applied field directions. To achieve the correct weighting, each calculated spectrum was normalized by a factor corresponding to the cosine of the angle between the crystallographic ab -plane and the direction of the applied magnetic field. For each fixed magnitude of applied magnetic field, we use the zero-field determined exchange con-

stants and vary the magnitude of the spin-canting angle to compare the calculated spectrum to the measured INS spectrum, using an additive background and overall multiplicative prefactor. The field-dependence of the spin-canting angle determined from this method is shown in the inset of Fig. 9. Here, the error bars correspond to an increase in reduced χ^2 by 2.5%. The resulting lineshapes drawn in Fig. 9 are in good agreement with the measured field-dependent spectra. Because of the anisotropy intrinsic to our sample, it is possible that a number of the grains of the powder would be rearranged by the applied magnetic field. To understand this possibility, we considered the spectrum in Fig. 9 as if the magnetic field was solely applied along the c -axis of the compound. From examination of the spin-wave scattering intensity, the c -axis component of magnetic field is mostly responsible for the shift in the density of magnetic states to lower energy transfers. In this case, the spin canting angle determined as a function of applied magnetic field is smaller than the random-field calculation, as is shown in the inset of Fig. 9. For both calculations, we find that the ordered magnetic moments gradually rotate from their zero-field orientation toward the applied magnetic field as a function of the applied magnetic field. The powder nature of the sample does not allow us to easily model the case of a distribution of ordered moment orientations. Considering a linear dependence for the ordered moment direction as a function of field for both models, the shaded range in the inset of Fig. 9 represents the most likely range of canting angles for different orientations of applied magnetic field.

Magnetic susceptibility The magnetic susceptibility (χ_{obs}) of $[\text{Ni}(\text{HF}_2)(\text{pyz})_2]\text{SbF}_6$ exhibits a broad maximum at 16 K associated with the formation of spin correlations along the Ni—FHF—Ni chains as the sample is cooled²⁷ [Fig. 10(a)]. There is a rapid decrease in χ_{obs} on reducing T through the ordering transition at 12.2 K and the susceptibility plateaus as T is decreased further. The data for $T \geq 10$ K are compared to a simulation of the susceptibility (χ_{sim}) using a 1D chain model⁷⁴ of $S = 1$ ions with intrachain exchange J and single-ion anisotropy D , which is expressed as:

$$\chi_{\text{sim}} = \frac{2\mu_0 N_A \mu_B^2 g^2}{3k_B J} \left[\frac{t^2 + 0.5t + 0.1}{a_3 t^3 + a_2 t^2 + a_1 t + a_0} \right] \quad (6)$$

where $t = \frac{T}{J}$ is the reduced temperature and the coefficients a_i are polynomials of the $\frac{D}{J}$ ratio:

$$a_i = \sum_{j=0}^2 c_{ij} \left(\frac{D}{J} \right)^j \quad (7)$$

with the coefficients c_{ij} given in Table VII. Eqn. 6 can be used to attempt fits of $\chi(T)$ data for powders.

Fixing the powder average g -factor to the published value²⁷, $g = 2.08$, the susceptibility (Eqn. 6) was simulated for parameters in the range $0 \leq D \leq 30$ K,

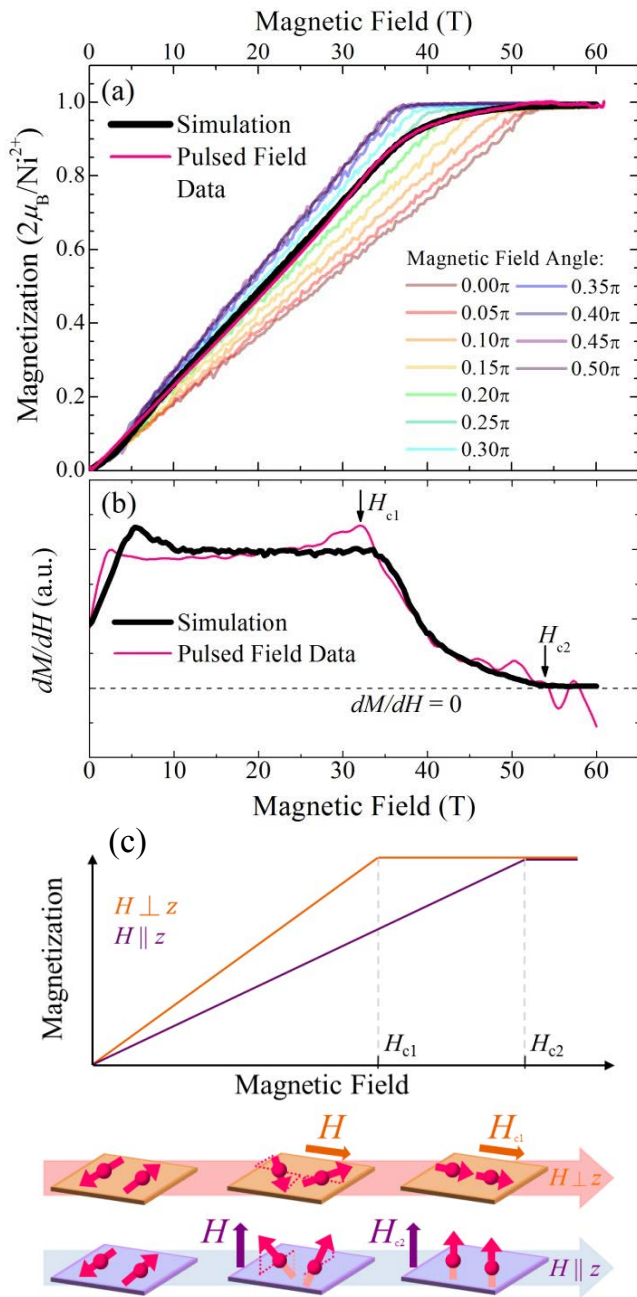


FIG. 11. (a) Simulated magnetization (M) versus magnetic field for $[\text{Ni}(\text{HF}_2)(\text{pyz})_2]\text{SbF}_6$ using a Monte-Carlo energy-minimization routine for an 8-spin cluster governed by Eqn. 1 with $D = 13.3$ K, $J = 10.3$ K, $J' = 1.43$ K and $g = 2.08$. Magnetization curves are obtained for 21 orientations of the magnetic field with respect to the hard axis (colored lines show the unique angles) and the powder-average M (black line) is determined from Eqn. 2. Good agreement with the $T = 0.56$ K pulsed-field M data (pink line) is achieved. (b) Differential susceptibility of $[\text{Ni}(\text{HF}_2)(\text{pyz})_2]\text{SbF}_6$ as deduced from the Monte-Carlo simulation (black line) compared with pulsed-field measurements (pink line). (c) Illustration of the field-induced spin reorientation that occurs when H is applied perpendicular or parallel to the z -axis.

TABLE VII. Coefficients (c_{ij} , Eqn. 7) for the polynomials (a_i , Eqn. 6) from Ref. 74.

Polynomial (a_i)	c_{i0}	c_{i1}	c_{i2}
$i = 0$	1.67268034	-0.26449121	-0.102945
$i = 1$	1.710151691	0.5114739	0.18853874
$i = 2$	1.899474528	-0.166396406	0.1494167
$i = 3$	1	0	0

$5 \leq J \leq 15$ K and $10 \leq T \leq 300$ K ($\Delta T = 1$ K). The quality factor

$$R = \frac{\sum_i |\chi_{\text{obs},i} - \chi_{\text{sim},i}|}{\sum_i \chi_{\text{obs},i}} \quad (8)$$

was computed for each simulated curve, where i runs over all data points for $T \geq 10$ K. A contour plot of R across the $D-J$ plane [Fig. 10(b)] reveals bands of D and J values that all produce χ_{sim} curves providing equally good representations of the measured data. This insensitivity of Eqn. 6 to a detuning of D and J from the minimum in R (white region) indicates that the results of fitting the susceptibility to Eqn. 6 should be treated with caution. The parameters D and J are strongly correlated, which likely results from their competing energy scale and the fact that a low-field bulk measurement of the susceptibility, as obtained from a powder sample, cannot differentiate between the effects of spatial exchange anisotropy and single-ion anisotropy for an $S = 1$ chain.

The values of D and J deduced from the mean-field analysis of the magnetization and the more precise results obtained by simulating the INS data (Fig. 10(b), triangles) both fall close to the white band in the contour map, indicating good consistency with the broad temperature dependence of the χ_{obs} data. The high-field magnetization and INS measurements, however, offer a significant advantage over the susceptibility analysis, as a single experiment can constrain both D and J . This results from two key differences in the techniques as compared to the low-field susceptibility measurements: (i) the high-field magnetization is sensitive to the anisotropy of the critical field; and (ii) a local probe such as neutron scattering is sensitive to the local symmetry of the magnetic centers and so a single experiment can constrain both D and J . Thus, the choice of a high-field or local experimental probe was crucial to differentiate the effects of spatial-exchange and single-ion anisotropy in the magnetic properties of this sample. Furthermore, the simulated susceptibility curve that minimizes R [Fig. 10(a), line] significantly deviates from the measured data in the ordered phase. For temperatures $T \leq T_c$, the effects of finite interchain interactions (J') may not be ignored and this further complicates the analysis of the susceptibility at low temperatures. Thus, we find that the local INS probe is necessary to efficiently and precisely determine the full set of magneto-structural parameters (D , J and J') for $[\text{Ni}(\text{HF}_2)(\text{pyz})_2]\text{SbF}_6$.

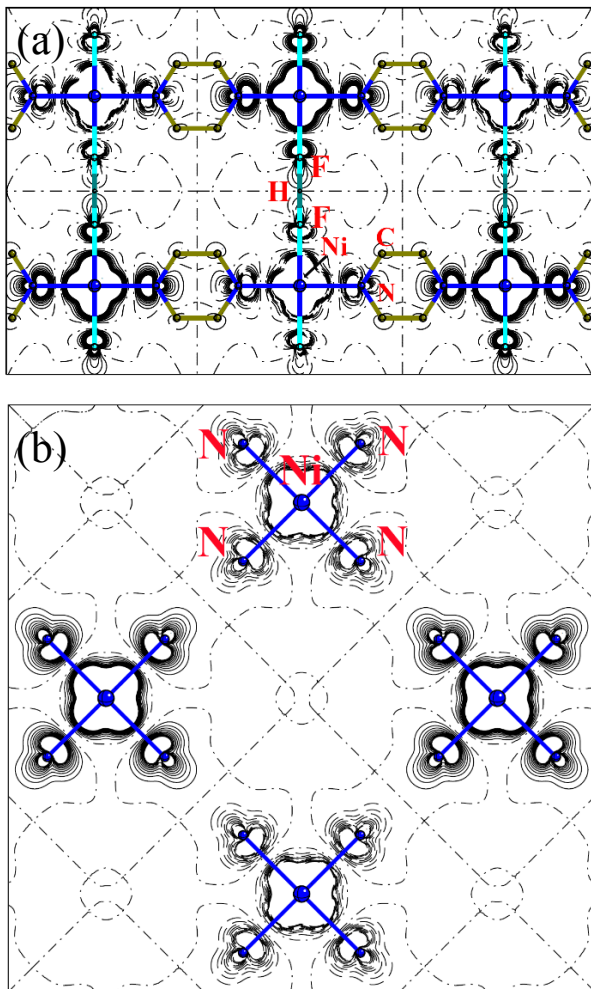


FIG. 12. The electron spin-density distribution in the (a) [110] and (b) [001] planes, calculated for the AFM state (solid and dashed lines represent the excess or defect of α spin-density; contours are drawn with a logarithmic increase). The spin density is delocalized along both ligand types. However, the spin delocalization is essentially quenched along Ni—pyz—Ni because only the σ skeleton is involved. In contrast, the spin delocalization is not disrupted along the Ni—FHF—Ni bridge.

C. Calculations and modeling

Monte-Carlo simulation of the magnetization. The magnetization of $[\text{Ni}(\text{HF}_2)(\text{pyz})_2]\text{SbF}_6$ was calculated from a Monte-Carlo energy minimization routine on an 8-spin cluster for 21 orientations of the applied field with respect to the magnetic hard-axis of the Ni(II) ions [Fig. 11(a), colored lines]. The critical field was found to be anisotropic, such that a greater applied field is required to saturate the moments as the field orientation is moved away from the easy-plane. The resultant powder-average magnetization was determined from Eqn. 2 (thick line) and compared to the measured magnetization at the lowest available temperature (pink line; $T = 0.56$ K).

TABLE VIII. Magnetic parameters from Eqn. 1 (in Kelvin) as deduced from high-field magnetization data and inelastic neutron-scattering (INS) experiments. For comparison, DFT-computed values are included in the last column. To decompose $n\langle J \rangle$ into individual J and J' contributions from the magnetization data it was necessary to infer an average value of J' from a catalog of related coordination polymers that also contain square $[\text{Ni}(\text{pyz})_2]^{2+}$ motifs (see Table VI).

Parameter (K)	$M(H)$ data	INS data	DFT
D	13.2(5)	13.3(1)	–
J	9.2(5)	10.4(3)	9.2
J'	0.9(2)	1.4(2)	1.8

An overall good agreement of the rounded approach towards saturation for the powdered sample is obtained. Furthermore, the parameters $D = 13.3$ K, $J = 10.3$ K, $J' = 1.43$ K and $g = 2.11$ yield a good quantitative agreement for the two observed critical fields [Fig. 11 (a)].

The measured pulsed-field magnetization develops a slight concavity on approaching H_{c1} with increasing field as the bath temperature is reduced below 8 K [Fig. 11(b)], which leads to a small rise in dM/dH at H_{c1} . This behavior is not reproduced by the simulation that employed classical vectors to represent the Ni(II) moments. The small discrepancy may be attributed to the development of quantum fluctuations of the $S = 1$ magnetic moments, which result from the Q1D nature of the spin-exchange interactions⁷⁵ that act to suppress the magnetization at low temperatures. Furthermore, the small rise in dM/dH evident close to 5 T in the simulated data is an artefact attributed to the finite number of cycles used to determine the ground state spin configuration. This ultimately causes a slight underestimation of the magnetization in this field regime⁷⁶.

Fig. 11(c) shows a schematic of the behavior expected for classical spins as the field is applied parallel and perpendicular to the hard axis, with anisotropic critical fields indicated. In real Q1D $S = 1$ systems the magnetization at fields less than H_c will not be a linear function of field; instead the reduced dimensionality gives rise to a concavity in the single-crystal $M(H)$ data, as captured by quantum Monte Carlo simulations⁷⁵.

Theoretical spin-density distribution. Periodic DFT calculations on $[\text{Ni}(\text{HF}_2)(\text{pyz})_2]\text{SbF}_6$ enabled us to estimate the J and J' exchange constants by calculating the energy of the FM state and of two different AFM states, with spin pairing along the c -axis (AFM_{FHF}) or in the ab -plane (AFM_{pyz}), as well as the full AFM state with both kinds of pairing (Fig. S2). The energy difference ΔE between the FM and the AFM_{FHF} or AFM_{pyz} states can be used to calculate J or J' , respectively, using Eqn. 1 and assuming the calculated ΔE to be equivalent to the result of the corresponding Heisenberg Hamiltonian. The primary J can also be obtained from $E(\text{AFM}) - E(\text{AFM}_{\text{pyz}})$, whereas J' can be obtained from

$E(\text{AFM}) - E(\text{AFM}_{\text{FHF}})$. Considering the experimental geometries, both approaches provided $J = 9.2$ K and $J' = 1.8$ K, in good agreement with the model derived from INS. The calculated periodic wave function also enabled mapping of the spin-density distribution in all states. Fig. 12 shows the spin-density distribution of the AFM state. For all states (FM or AFM), the Ni atom bears $\approx 1.75e$ of excess spin. The remaining $0.25e$ is delocalized onto all ligands and are responsible for the observed magnetic exchange. Despite $J' \ll J$, the largest spin population lies on the pyrazine N-atom ($\approx 0.05e$), whereas only $0.02e$ reside on the F-atoms. This is certainly caused by N being a stronger donor than F^- (in accord with the spectrochemical series). However, because the exchange mechanism through pyrazine is mainly σ -type (as shown for some Cu-pyrazine networks)⁷⁷ it is not as effective for the magnetic exchange, which explains the smaller J' . The optimal delocalization via the pyrazine-bridge would occur through the π -electrons which are not significantly involved in the spin density. In fact, population analysis shows that the atomic p orbitals of N and C involved in the pyrazine π -system contribute very little to the overall spin density. On the other hand, the short F—F distance in the HF_2^- ligand likely promotes more effective spin delocalization, as clearly evident in Fig. 12(a).

V. CONCLUSIONS

The material $[\text{Ni}(\text{HF}_2)(\text{pyz})_2]\text{SbF}_6$ retains tetragonal symmetry for temperatures down to 1.5 K and may be characterized as a Q1D $S = 1$ quantum magnet that exhibits a 3D XY -AFM ground state below 12.2(1) K as determined from high-resolution elastic neutron scattering. The magnetic properties can be described by the Hamiltonian in Eqn. 1, with $D = 13.3(1)$ K, $J = 10.3(3)$ K and $J' = 1.4(2)$ K as determined by INS measurements. We showed that these values are in reasonable agreement with the initial estimates deduced from high-field magnetization studies (see Table VIII), while low-field bulk thermodynamic probes such as magnetic susceptibility were unable to satisfactorily untangle the effects of the spatial exchange and single-ion anisotropies. Compared to the previous study²⁷, the DFT results presented in this work more closely agree with the experimentally derived J and J' parameters.

The predicted¹² phase diagram for easy-plane ($D > 0$) Q1D spin-1 systems is shown in Fig. 13. The phase boundaries, as deduced from QMC calculations, separate regions of XY AFM order from the disordered quantum paramagnetic and Haldane phases; the three phases converge¹² at the quantum critical point $\frac{D}{J} = 0.97$. The relative position of $[\text{Ni}(\text{HF}_2)(\text{pyz})_2]\text{SbF}_6$ is indicated on the phase diagram both the precise J'/J and D/J ratios from INS and those estimated from a mean-field analysis of the critical fields observed in pulsed-field magnetization. Both estimates predict $[\text{Ni}(\text{HF}_2)(\text{pyz})_2]\text{SbF}_6$ to exhibit an XY -AFM ground state, though only INS independently determined all three parameters needed to validate this prediction. The lack of a gapped ground state is in full agreement with both the field-dependent heat capacity, which showed clear evidence of a transition to an AFM ground state, and the refined magnetic structure from elastic neutron scattering in zero field.

Given the proximity of $[\text{Ni}(\text{HF}_2)(\text{pyz})_2]\text{SbF}_6$ to the quantum-critical point and phase boundaries to two other distinct phases, this material is an intriguing candidate for a pressure-dependent study to determine the extent to which the parameters D , J and J' can be tuned to explore the phase diagram and further test the predictions of QMC simulations for Q1D $S = 1$ systems. While there is no substitute for the detailed study of single crystals, the success of this work on powder samples demonstrates the complementary capabilities of the micro- and macroscopic probes involved. More specifically, the experimental sequence was as follows: (i) micro-crystal synchrotron X-ray diffraction determines the crystal structure; (ii) using this structure as a starting point, an analysis of the powder elastic-neutron diffraction establishes the magnetic ground state and charts the evolution of the ordered moment as a function of temperature; (iii) using the magnetic structure as the starting point, an analysis of the powder inelastic-neutron scattering determines the magnetic exchange and anisotropy parameters; (iv) an independent estimate of the mag-

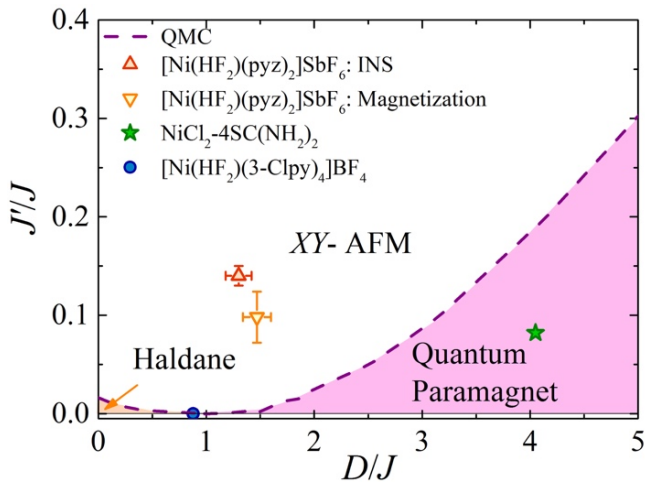


FIG. 13. Phase diagram of $S = 1$ Q1D materials as a function of intrachain exchange (J), interchain interaction (J') and single-ion anisotropy (D). The phase boundaries are the results of quantum Monte-Carlo calculations¹². The position of $[\text{Ni}(\text{HF}_2)(\text{pyz})_2]\text{SbF}_6$ as determined from both pulsed-field magnetization and INS (triangles) predicts the material to have an antiferromagnetic XY -ordered ground state. The positions of the quantum paramagnet⁷ $\text{NiCl}_2\text{-4SC}(\text{NH}_2)_2$ (star) and Haldane-chain system¹¹ $[\text{Ni}(\text{HF}_2)(3\text{-Clpy})_4]\text{BF}_4$ (circle) are included for comparison.

netic parameters was possible via a careful analysis of the high-field powder magnetometry data and was found to be in good agreement with the results of the neutron scattering; (v) the field-temperature phase diagram was mapped out using high-field-magnetization and heat-capacity measurements. Having established the applicability of the methodology, we are currently applying this experimental protocol to other $S = 1$ materials.

VI. ACKNOWLEDGMENTS

The work at EWU was supported by the National Science Foundation (NSF) under grant no. DMR-1306158 and by the National Institute of Standards and Technology (NIST) Cooperative Agreement 70NANB15H262. ChemMatCARS Sector 15 is principally supported by the Divisions of Chemistry (CHE) and Materials Research (DMR), NSF, under grant no. CHE-1346572. Use of the Advanced Photon Source, an Office of Science User Facility operated for the U.S. Department of Energy (DoE) Office of Science by Argonne National Laboratory, was supported by the U.S. DoE under Contract No. DE-AC02-06CH11357. We acknowledge the support of NIST, U.S. Department of Commerce (DoC), in providing their neutron research facilities used in this

work; identification of any commercial product or trade name does not imply endorsement or recommendation by NIST. Work performed at the National High Magnetic Field Laboratory, USA, was supported by NSF Cooperative Agreement DMR-1157490, the State of Florida, U.S. DoE, and through the DoE Basic Energy Science Field Work Project Science in 100 T. M.B.S. was supported by the Scientific User Facilities Division, Office of Basic Energy Sciences, U.S. Department of Energy. We gratefully acknowledge the ISIS-RAL facility for the provision of beamtime. J.B. thanks EPSRC for financial support. P.A.G. acknowledges that this project has received funding from the European Research Council (ERC) under the European Union's Horizon 2020 research and innovation programme (grant agreement No. 681260). Research at the University of Bern was funded by the Swiss NSF (project 160157). J.S. acknowledges a Visiting Professorship from the University of Oxford that enabled some of the experiments reported in this paper.

‡Contact email: J.D.Brambleby@warwick.ac.uk

*Contact email: jmanson@ewu.edu

ℵContact email: jsingle@lanl.gov

-
- ¹ J.M. Kosterlitz and D.J. Thouless, *J. Phys. C: Solid State* **5**, L124 (1972).
- ² J.M. Kosterlitz and D.J. Thouless, *J. Phys. C: Solid State* **6**, 1181 (1973).
- ³ F.D.M. Haldane, *Phys. Lett. A* **93**, 464 (1983).
- ⁴ F.D.M. Haldane, *Phys. Rev. Lett.* **50**, 1153 (1983).
- ⁵ *The Nobel Prize in Physics 2016 Advanced Information*. Nobelprize.org. Nobel Media AB 2014. <http://www.nobelprize.org/nobel_prizes/physics/laureates/2016/advanced.html>
- ⁶ A. Paduan-Filho, X. Gratens, N.F. Oliveira *Phys. Rev. B* **69**, 020405R (2004).
- ⁷ V.S. Zapf, D. Zocco, B.R. Hansen, M. Jaime, N. Harrison, C.D. Batista, M. Kenzelmann, C. Niedermayer, A. Lacerda, A. Paduan-Filho, *Phys. Rev. Lett.* **96**, 077204 (2006).
- ⁸ L. Yin, J.-S. Xia, V.S. Zapf, N.S. Sullivan, A. Paduan-Filho, *Phys. Rev. Lett.* **101**, 187205 (2008).
- ⁹ J.P. Renard, M. Verdaguer, L.P. Regnault, W.A.C. Erkelens, J. Rossat-Mignod, W.G. Stirling, *Europhys. Lett.* **3**, 945 (1987).
- ¹⁰ J.L. Manson, A.G. Baldwin, B.L. Scott, J. Bendix, R.E. Del Sesto, P.A. Goddard, Y. Kohama, H.E. Tran, S. Ghanadzadeh, J. Singleton, T. Lancaster, J.S. Möller, S.J. Blundell, F.L. Pratt, V.S. Zapf, J. Kang, C. Lee, M.-H. Whangbo, C. Baines, *Inorg. Chem.* **51**, 7520 (2012).
- ¹¹ J.-S. Xia, A. Ozarowski, P.M. Spurgeon, A.C. Baldwin, J.L. Manson, M.W. Meisel, arXiv:1409.5971 (2014).
- ¹² K. Wierschem, P. Sengupta *Mod. Phys. Lett. B* **28**, 1430017 (2014) and refs. therein.
- ¹³ S. Sachdev, B. Keimer, *Phys. Today* **64**, 29 (2011).
- ¹⁴ R. Boča, *Coord. Chem. Rev.* **248**, 757 (2004).
- ¹⁵ J.L. Manson, A. Ozarowski, S.H. Lapidus, J.A. Villa, A. Sarkar, S. Saeidi, M.W. Meisel, preprint (2016).
- ¹⁶ W. J. Blackmore *et al.* (in preparation).
- ¹⁷ T. Chatterji, (Ed.) *Neutron Scattering from Magnetic Materials* (Elsevier Science, London, 2006).
- ¹⁸ O. Pieper, T. Guidi, S. Carretta, J. van Slageren, F. El Hallak, B. Lake, P. Santini, G. Amoretti, H. Mutka, M. Koza, M. Russina, A. Schnegg, C.J. Milios, E.K. Brechin, A. Julià, J. Tejada, *Phys. Rev. B* **81**, 174420 (2010).
- ¹⁹ H. Andres, R. Basler, H.-U. Güdel, G. Aromi, C. Christou, H. Büttner, B. Rufflé, *J. Amer. Chem. Soc.* **122**, 12469 (2000).
- ²⁰ A.B. Boer, A.-L. Barra, L.F. Chibotaru, D. Collison, E.J.L. McInnes, R.A. Mole, G.G. Simeoni, G.A. Timco, L. Ungur, T. Unruh, R.E.P. Winpenny, *Angew. Chem. Int. Ed.* **50**, 4007 (2011).
- ²¹ K.G. Alley, R. Bircher, O. Waldmann, S.T. Ochsenein, H.-U. Güdel, B. Moubaraki, K.S. Murray, F. Fernandez-Alonso, B.F. Abrahams, C. Boskovic, *Inorg. Chem.* **45**, 8950 (2006).
- ²² J.M. Clemente-Juan, E. Coronado, A. Gaita-Ariño, C. Saiz-Giménez, H.-U. Güdel, A. Sieber, R. Bircher, H. Mutka, *Inorg. Chem.* **44**, 3389 (2005).
- ²³ J.L. Manson, Q.-Z. Huang, C.M. Brown, J.W. Lynn, M.B. Stone, J. Singleton, F. Xiao, *Inorg. Chem.* **54**, 11897 (2015).
- ²⁴ B.J. Houghton, R.J. Deeth, *Eur. J. Inorg. Chem.* **2014**, 4573 (2014).
- ²⁵ A.J. Cohen, P. Mori-Sanchez, W. Yang, *Chem. Rev.* **112**, 289 (2012).

- ²⁶ F. Neese, *Coord. Chem. Rev.* **253**, 526 (2009).
- ²⁷ J.L. Manson, S.H. Lapidus, P.W. Stephens, P.K. Peterson, K.E. Carreiro, H.I. Southerland, T. Lancaster, S.J. Blundell, A.J. Steele, P.A. Goddard, F.L. Pratt, J. Singleton, Y. Kohama, R.D. McDonald, R.E. Del Sesto, N.A. Smith, J. Bendix, S.A. Zvyagin, J. Kang, C. Lee, M.-H. Whangbo, V.S. Zapf, A. Plonczak, *Inorg. Chem.* **50**, 5990 (2011).
- ²⁸ S. Toth, B. Lake, *J. Phys. Condens. Matter* **27**, 166002 (2015).
- ²⁹ J.L. Manson, K.E. Carreiro, S.H. Lapidus, P.W. Stephens, P.A. Goddard, R.E. Del Sesto, J. Bendix, S. Ghannadzadeh, I. Franke, J. Singleton, T. Lancaster, J.S. Möller, P.J. Baker, F.L. Pratt, S.J. Blundell, J. Kang, C. Lee, M.-H. Whangbo, *Dalton Trans.* 2012, **41**, 7235 (2012).
- ³⁰ J. Brambleby, P.A. Goddard, R.D. Johnson, J. Liu, D. Kaminski, A. Ardavan, A.J. Steele, S.J. Blundell, T. Lancaster, P. Manuel, P.J. Baker, J. Singleton, S. Schwalbe, P.M. Spurgeon, H.E. Tran, P.K. Peterson, J.F. Corbey, J.L. Manson, *Phys. Rev. B* **92**, 134406 (2015).
- ³¹ J.L. Manson, M.M. Conner, J.A. Schlueter, T. Lancaster, S.J. Blundell, M.L. Brooks, F.L. Pratt, T. Papageorgiou, A.D. Bianchi, J. Wosnitza, M.-H. Whango, *Chem. Commun.* **2006**, 4894 (2006).
- ³² J.L. Manson, H.I. Southerland, B. Twamley, R. Rai, J.L. Musfeldt, *Dalton Trans.* **2007**, 5655 (2007).
- ³³ P.A. Goddard, J. Singleton, P. Sengupta, R.D. McDonald, T. Lancaster, S.J. Blundell, F.L. Pratt, S. Cox, N. Harrison, J.L. Manson, H.I. Southerland, J.A. Schlueter, *New J. Phys.* **10**, 083025 (2008).
- ³⁴ J.L. Manson, J.A. Schlueter, K.A. Funk, H.I. Southerland, B. Twamley, T. Lancaster, S.J. Blundell, P.J. Baker, F.L. Pratt, J. Singleton, R.D. McDonald, P.A. Goddard, P. Sengupta, C.D. Batista, L. Ding, C. Lee, M.-H. Whangbo, I. Franke, S. Cox, C. Baines, D. Trial, J. Amer. Chem. Soc. **131**, 6733 (2009).
- ³⁵ E. Čížmár, S.A. Zvyagin, R. Beyer, M. Uhlarz, M. Ozerov, Y. Skourski, J.L. Manson, J.A. Schlueter, J. Wosnitza, *Phys. Rev. B* **81**, 064422 (2010).
- ³⁶ J.L. Manson, M.L. Warter, J.A. Schlueter, T. Lancaster, A.J. Steele, S.J. Blundell, F.L. Pratt, J. Singleton, R.D. McDonald, C. Lee, M.-H. Whangbo, A. Plonczak, *Angew. Chem. Int. Ed.* **50**, 1573 (2011).
- ³⁷ W. Li, M.S.R.N. Kiran, J.L. Manson, J.A. Schlueter, A. Thirumurugan, U. Ramamurty, A.K. Cheetham, *Chem. Commun.* **49**, 4471 (2013).
- ³⁸ S.H. Lapidus, J.L. Manson, H. Park, A.J. Clement, S. Ghannadzadeh, P.A. Goddard, T. Lancaster, J.S. Möller, S.J. Blundell, M.T.F. Telling, J. Kang, M.-H. Whangbo, J.A. Schlueter, *Chem. Commun.* **49**, 499 (2013).
- ³⁹ S. Ghannadzadeh, J.S. Möller, P.A. Goddard, T. Lancaster, F. Xiao, S.J. Blundell, A. Maisuradze, R. Khasanov, J.L. Manson, S.W. Tozer, D. Graf, J.A. Schlueter, *Phys. Rev. B* 2013, **87**, 241102R (2013).
- ⁴⁰ C.H. Wang, M.D. Lumsden, R.S. Fishman, G. Ehlers, T. Hong, W. Tian, H. Cao, A. Podlesnyak, C. Dunmars, J.A. Schlueter, J.L. Manson, A.D. Christianson, *Phys. Rev. B* **86**, 064439 (2012).
- ⁴¹ A. Prescimone, C. Morien, D. Allan, J.A. Schlueter, S.W. Tozer, J.L. Manson, S. Parsons, E.K. Brechin, S. Hill, *Angew. Chem. Int. Ed.* **51**, 7490 (2012).
- ⁴² G.J. Halder, K.W. Chapman, J.A. Schlueter, J.L. Manson, *Angew. Chem. Int. Ed.* **50**, 419 (2011).
- ⁴³ J.L. Musfeldt, Z. Liu, S. Li, J. Kang, C. Lee, P. Jena, J.L. Manson, J.A. Schlueter, G.L. Carr, M.-H. Whangbo, *Inorg. Chem.* **50**, 6347 (2011).
- ⁴⁴ J.L. Manson, M.M. Conner, J.A. Schlueter, A.C. McConnell, H.I. Southerland, I. Malfant, T. Lancaster, S.J. Blundell, M.L. Brooks, F.L. Pratt, J. Singleton, R.D. McDonald, C. Lee, M.-H. Whangbo, *Chem. Mater.* **20**, 7408 (2008).
- ⁴⁵ Caution! Hydrofluoric acid must be handled with great care as it is highly toxic, corrosive, and will cause severe burns. Proper personal protective equipment must be worn at all times regardless of the amount of HF being used.
- ⁴⁶ See Supplementary Information, appended to this paper.
- ⁴⁷ SAINT v8.34A; Bruker AXS Inc.: Madison, WI, 2013
- ⁴⁸ SADABS v.2014/15; Bruker AXS Inc.: Madison, WI, 2014
- ⁴⁹ SHELXT v.2014/4; Bruker AXS Inc.: Madison, WI, 2014
- ⁵⁰ SHELXL v.2014/7; Bruker AXS Inc.: Madison, WI, 2014
- ⁵¹ International Tables for Crystallography (2006). Vol. A, part 7, pp. 448-449.
- ⁵² L. Chapon, P. Manuel, P. Radaelli, C. Benson, L. Penot, S. Ansell, N. Rhodes, D. Raspino, D. Duxbury, E. Spill, J. Norris, *Neutron News* **22**, 22 (2011).
- ⁵³ J. Rodriguez-Carvajal, *Physica (Amsterdam)* **192**, 55 (1993).
- ⁵⁴ J. Lashley, M.F. Hundley, A. Migliori, J.L. Sarrao, P.G. Pagliuso, T.W. Darling, M. Jaime, J.C. Cooley, W.L. Hults, L. Morales, D. Thoma, J.L. Smith, J. Boerio-Goates, B.F. Woodfield, G.R. Stewart, R.A. Fisher, N.E. Phillips, *Cryogenics* **43**, 369 (2003).
- ⁵⁵ J. Copley, *Physica B* **180-181**, 914 (1992).
- ⁵⁶ MATLAB v.8.0.0.783; The Math Works, Inc.: Natick, MA, 2012
- ⁵⁷ D.P. Landau, K. Binder, *A Guide to Monte Carlo Simulations in Statistical Physics*, 3rd Ed.; (Cambridge University Press, Cambridge, 2009) pp. 68-137.
- ⁵⁸ L.J. Noodleman, *Chem. Phys.* **74**, 5737 (1981).
- ⁵⁹ L.J. Noodleman, E.R. Davidson, *Chem. Phys.* **109**, 131 (1986).
- ⁶⁰ M. Deumal, M.J. Bearpark, J.J. Novoa, M.A. Robb, *J. Phys. Chem. A* **106**, 1299 (2002).
- ⁶¹ E. Ruiz, J. Cano, S. Alvarez, P.J. Alemany, *J. Comput. Chem.* **20**, 1391 (1999).
- ⁶² R. Dovesi, V.R. Saunders, C. Roetti, R. Orlando, C.M. Zicovich-Wilson, F. Pascale, B. Civalleri, K. Doll, N.M. Harrison, I.J. Bush, P. D'Arco, M. Llunell, M. Causà, Y. Noël, *CRYSTAL14 Users Manual*. (University of Torino, Torino 2014).
- ⁶³ P.C. Hariharan, J.A. Pople, *Theor. Chim. Acta* **28**, 213 (1973).
- ⁶⁴ K.D. Dobbs, W.J. Hehre, *J. Comput. Chem.* **8**, 880 (1987).
- ⁶⁵ R.S. Mulliken, *J. Chem. Phys.* **23**, 1833 (1955).
- ⁶⁶ J. Liu, P.A. Goddard, J. Singleton, J. Brambleby, F. Foronda, J.S. Möller, Y. Kohama, S. Ghannadzadeh, A. Ardavan, S.J. Blundell, T. Lancaster, F. Xiao, R.C. Williams, F.L. Pratt, P.J. Baker, K. Wierschem, S.H. Lapidus, K.H. Stone, P.W. Stephens, J. Bendix, M.R. Lees, T.J. Woods, K.E. Carreiro, H.E. Tran, C.J. Villa, J.L. Manson, *Inorg. Chem.* **55**, 3515 (2016); and unpublished results.
- ⁶⁷ F. Lloret, M. Julve, J. Cano, G. De Munno, *Mol. Cryst. Liq. Cryst.* **334**, 569 (1999).
- ⁶⁸ R.F. Wiliams, *Prog. Low Temp. Phys.* Vol. VI, p. 333 (North Holland, Amsterdam, 1970).
- ⁶⁹ M. Sorai, M. Nakano, Y. Miyazaki, *Chem. Rev.* **106**, 976 (2006).

- ⁷⁰ We refer to the ordering temperature as T_c , rather than T_N , as our system is not a conventional Néel antiferromagnet.
- ⁷¹ W.J.A. Blackmore, J. Brambleby, P.A. Goddard, M. Healey, B. Slater, J. Singleton, A. Ozarowski, J.A. Schlueter, S.H. Lapidus, J.A. Villa, D.Y. Villa, J.L. Manson, in preparation (2016).
- ⁷² M.B. Stone, G. Ehlers, G. Granroth, *Phys. Rev. B* **88**, 104413 (2013).
- ⁷³ M.B. Stone, M.D. Lumsden, Y. Qiu, E.C. Samulon, C.D. Batista, I.R. Fisher, *Phys. Rev. B* **77**, 134406 (2008).
- ⁷⁴ J.J. Borrás-Almenar, E. Coronado, J. Curely, R. Georges, *Inorg. Chem.* **34**, 2699 (1995).
- ⁷⁵ K. Wierschem, P. Sengupta, *J. Phys.: Conf. Ser.* **400**, 032112 (2012).
- ⁷⁶ At low fields, where the number of degenerate ground states in the uniaxial system is greatest, running a finite length Monte-Carlo Markov chain simulation to iterate an ensemble of spins towards their ground state configuration can lead to a small proportion of the spins ending up perturbed from their lowest energy orientation. Through averaging the final magnetization over many repeated simulations performed in this manner, this can lead to an underestimation of the magnetization and the slight kink in M versus H as found in the simulated traces.
- ⁷⁷ L.H.R. Dos Santos, A. Lanza, A.M. Barton, J. Brambleby, W.J.A. Blackmore, P.A. Goddard, F. Xiao, R.C. Williams, T. Lancaster, F.L. Pratt, S.J. Blundell, J. Singleton, J.L. Manson, P. Macchi, *J. Amer. Chem. Soc.* **138**, 2280 (2016).